Temperature–time relationships and their implications for thermal history and modelling of silica diagenesis in deep-sea sediments

Shahab Varkouhi[1], Nicholas J. Tosca[2], and Joseph A. Cartwright[1]

1 Department of Earth Sciences, University of Oxford, Oxford, UK

2 Department of Earth Sciences, University of Cambridge, Cambridge, UK

ABSTRACT

67 Ocean Drilling Program and Deep Sea Drilling Project sites were investigated to determine the relationship between temperature and time for silica diagenesis. The selected sites cover a variety of settings where the opal-A to opal-CT transition zone lies in Cenozoic sediments. The opal-A to opal-CT transition leads to abrupt changes in the sediment petrophysics which are used to identify the diagenetic interval at the study sites. This transition zone is a thin interval ranging in thickness from 10 to 40 m. Controls on transition zone thickness are analysed and temperature was found to be the fundamental driver. This study extends "the time–temperature stability field of Hein et al. (1978)" for the onset of opal-CT precipitation more generally. Active silica diagenesis persists over a long period of time (> 35 m.y.) at low temperatures (< 30 °C), within 3 m.y. at moderate temperatures (35–55 °C), and much more rapidly at high temperatures (> 55 °C) regardless of burial depth. Geothermal gradients and sediment accumulation rates are the principal controls of the rate of silica diagenesis transformation. Sites 794 and 795 in the Japan Sea, as typical cases

of deep-sea boreholes capturing active transitions, were selected for further understanding the temperature–time control on silica diagenesis. The reconstructed thermal evolution of sediments from these representative sites demonstrates that the rapid increase in temperatures from the Late Miocene onwards occurred in response to high accumulation rates in the opal-A interval. The higher burial temperatures achieved for the opal-A sediment under higher sedimentation rates and a steeper thermal gradient led to an earlier transition at Site 795 (~5 m.y.) as compared to Site 794 (~8 m.y.). Kinetic-based models are formulated to illustrate the time–temperature dependence of biogenic silica diagenesis. One of the main findings based on this model is that although opal-CT precipitation reaches its peak levels across the transition zone at 8 and 5 m.y. after initial deposition of opal-A at Sites 794 and 795, respectively, the transformation is not completed until 14 m.y. at Site 794 and ca. 9.5 m.y. at Site 795 after initial sedimentation. Given the temperature and elapsed time, the model allows the transformation state of opal-containing sediments to be successfully predicted at any depth in these two sites.

Keywords: Biogenic silica diagenesis; Ocean Drilling Program; Deep Sea Drilling Project; Opal-A; Opal-CT

1. Introduction

Biogenic opal-A (also referred to as biogenic silica; e.g., Mortlock and Froelich, 1989) is diagenetically a metastable hydrous amorphous silica polymorph with sub-microscopic pores. It is usually produced by silica-secreting microorganisms,

specifically diatoms, radiolaria, silicoflagellates, and siliceous sponges. With burial, opal-A dissolves and reprecipitates as metastable opal-CT (cristobalite and tridymite) (e.g., Wise et al., 1972; Murata and Nakata, 1974; Kastner et al., 1977; Leeder, 1982; Williams and Crerar, 1985; Williams et al., 1985; Tada, 1991; Chaika and Williams, 2001; Weller and Behl, 2015). These diagenetic transformation processes lead to the formation and development of an opal-A to opal-CT transition zone ($TZ_{A/CT}$) in sediment records. This transition zone is often tens of metres in thickness (commonly <50 m thick; see Varkouhi, 2018; Varkouhi et al., 2020a) across which opal-A and opal-CT co-exist, though mostly composed of opal-CT. As a result of the transformation of biogenic silica to diagenetic opal-CT, petrophysical state of opal-A sediments changes sharply and significantly across the $TZ_{A/CT}$ (in particular a dramatic porosity reduction and marked density increases; e.g., Isaacs, 1981; Tada, 1991; Nobes et al., 1992; Chaika and Dvorkin, 1997; Meadows and Davies, 2007). Other abrupt physical variations associated with porosity and density changes at the depth of $TZ_{A/CT}$ include velocity and resistivity increases (Nobes et al. 1992), permeability reduction (Shipboard Scientific Party 1990a), pore-water loss (Isaacs 1981), and opal mass transfer (Tada 1991; Davies 2005).

The sharp contrasts between the petrophysical properties of these two silica polymorphs (opal-A and opal-CT) strongly control the overall character of the sediment. For instance, sediments rich in opal-A are commonly identified by their high porosity. As such, the $TZ_{A/CT}$ is mostly characterised by a dramatic reduction in porosity (or increase in density) (e.g., after Nobes et al., 1992; Chaika, 1998; Chaika

and Dvorkin, 2000; Davies and Cartwright, 2002; Davies et al., 2008; Meadows and Davies, 2010; Neagu, 2011; Weller and Behl, 2015). The abrupt decrease in the porosity of silica-rich rocks at these transitions is due to sudden anomalous compaction under the *in situ* dissolution of opal-A, allowing for compactional collapse of the sediment matrix supporting the porous structure of siliceous frustules (after Isaacs, 1981; also see Varkouhi, 2018; Varkouhi et al., 2020a).

The dissolution–reprecipitation pathway involved in the diagenetic inversion from opal-A toward opal-CT (and eventually to quartz) is controlled by temperature (burial depth), geological time (age), the potential roles of Al, Fe, Mg, and alkalinity, the surface area of biosilica, parent lithology, and the microbial decomposition of organic matter (e.g., Kastner et al., 1977; Hein et al., 1978; Iler, 1979; Williams and Crerar, 1985; Williams et al., 1985; Zijlstra, 1987; Nobes et al., 1992; Zijlstra; 1994; Hinman, 1990, 1998; Jurkowska and Świerczewska-Gładysz, 2020a, b). Among these, burial temperature and time are thought to be dominant drivers of silica diagenetic transformation through exerting controls over kinetic dissolution of biogenic opal in the sediment (e.g., after Mizutani, 1970; Kastner et al., 1977; Kastner and Gieskes, 1983; Williams and Crerar, 1985; Williams et al., 1985; Kuramoto et al., 1992; Nobes et al., 1992; Dove and Rimstidt, 1994; Hinman, 1998; Hesse and Schacht, 2011).

The interactions of temperature and time in silica diagenesis have been studied over the past five decades (Mizutani, 1970; Mizutani, 1977; Hein et al., 1978; Pisciotto,

1981a, 1981b; Pisciotto et al., 1992; Kastner and Gieskes, 1983; Wrona et al., 2017). The dependence of the silica diagenetic reactions on the thermal history of sediments (temperature vs time) was first stressed by Mizutani (1977) and experiments of Kastner et al. (1977). The current view is that the transformation of opal-A to opal-CT occurs at lower temperatures in older sediments, while higher temperatures are required in younger successions. Hein et al. (1978) estimated the time and temperature of this transformation reaction for moderately to highly biosiliceous Cenozoic deposits, and defined a diagrammatic temperature–time stability field for the formation of diagenetic silica.

Although the inverse relationship between temperature and time in ocean sediment settings is intuitive, we lack sufficient quantitative data to permit the prediction of silica diagenesis in response to both time and temperature. For example, Hein et al.'s (1978) stability field for the opal-A to opal-CT transformation was based only on six data points. Furthermore, noted mismatches between their diagram and data derived from comparable studies at Ocean Drilling Program (ODP) sites (e.g., Neagu, 2011) suggest a need to update this relationship and provide a more comprehensive model.

Predicting temperature–time relationships for biogenic silica diagenesis has implications for the reconstruction of the geothermal evolution of depositional basins accommodating the opal-A to opal-CT transformation. This also affects the determination of the likely diagenetic status of a $TZ_{A/CT}$, i.e., active versus arrested transition zones. Silica diagenetic reactions occur over thermodynamically active

transitions, in motion recently relative to the host lithology, at a recognisable rate (after Neagu et al., 2010); this is known from the discordant stratigraphic relationships between the $TZ_{A/CT}$ and its host strata (Meadows and Davies, 2007). Conversely, the opal-A to opal-CT conversion has been stopped in the arrested fronts (also referred to as fossilised fronts; e.g., Davies and Cartwright, 2002), i.e., cessation of silica diagenetic reactions across the transition zone. The structural criteria nominated by a few works in the past two decades (Roaldset and He, 1995; Brekke, 2000; Davies and Cartwright, 2002; Cartwright, 2007; Neagu et al., 2010) suggest that the silica reaction fronts are unlikely to remain active in their present-day sub-seabed position. Based on these studies, association of a $TZ_{A/CT}$ with three deformation styles, including polygonal faulting, antiforms/synforms, and differential folding indicates that silica diagenesis at this reaction boundary has been possibly arrested at a regional scale (Varkouhi et al., 2020b). These structural deformation modes have been particularly investigated by Neagu et al. (2010) on the seismic section of the mid-Norwegian continental margin. The throw value at the $TZ_{A/CT}$ hosted by the Neogene biosilica for each extensional polygonal fault is lower than the structural throw of accommodating lithology for the same fault. Neagu et al. (2010) ascribe this feature to the cease of the transition, probably since the late Miocene, prior to the last faulting episode on the mid-Norwegian margin. The folded geometry of the boundary indicates different temperature histories endured by its distinct deformed sections (Neagu et al., 2010). The structural ordering of diagenetic opal at the anticline crest is therefore less than that at the syncline trough as the depressed parts of the folded transition zone tolerate higher temperatures. As a result,

the maturity lines of opal-CT cross the modern isotherms, an indication for an arrested diagenesis (Mizutani, 1977; Varkouhi et al., 2020b). The uncommon domal folds (ridge–depression structures) formed across parts of this $TZ_{A/CT}$ have been attributed to the upward differential migration of the boundary and to the anomalous compaction this would entail. This explanation implies that the growth of domal folded morphology occurred as the reaction boundary distinctly advanced through the opal-A-rich sediment overburden. The well-ordered upward decrease in structural relief of the ridge–depression features agrees with the distinctive porosity drop and strongly suggests that the active upward migration of the $TZ_{A/CT}$ stopped prior to the last phase of biosilica deposition overlying this transition (Davies, 2005).

Given the significance of temperature–time relationships for transformation of biogenic to diagenetic opal, the underlying aim of this study therefore is to investigate the influence of thermal variations over time on buried sediment during this diagenetic process. The main goals of this study are threefold: (1) to extend the time–temperature domain of opal-CT stability diagram, (2) to approximate the thermal history of silica diagenesis, and (3) to model the early burial transformation of amorphous silica to opal-CT.

To achieve these goals, our work mines the ODP and Deep Sea Drilling Project (DSDP) databases. The $TZ_{A/CT}$ has been drilled through by more than 100 ODP and DSDP boreholes, distributed worldwide. From these locations, we have selected 67 sites where the $TZ_{A/CT}$ is recovered in the Cenozoic (Pliocene to Palaeocene) deep-sea

core deposits (Fig. 1). For most of these sites, multiple parameters (e.g., petrophysical and thermal parameters of the sediment hosting the $TZ_{A/CT}$ as well as the $TZ_{A/CT}$ characteristics) are available to act as indicators of silica diagenesis. We use these datasets to identify the $TZ_{A/CT}$ in the sediment records and to derive the data required for discussions on temperature–time relationships, and their implications for reconstruction of thermal history and modelling of biogenic silica diagenesis in deep-sea sediments. As the temperature domain of silica diagenesis can be deduced based on the thickness and depth of the $TZ_{A/CT}$ (Neagu, 2011), this manuscript also reports and discusses, in a preliminary way, variations observed in terms of the thickness of the transition zone and its controlling factors.

2. Depositional setting

Almost 3/4 out of the chosen sixty-seven ODP and DSDP borehole sites were drilled along the continental margins of North and South America, western-northwestern Africa, and east-southeast Asia (Fig. 1). The remaining sites are located mostly within Oceania and the Southern Ocean. The study sites represent marine depositional environments with highly porous biosiliceous uppermost sediments that shift abruptly and markedly to less-permeable lower porosity lithologic units deeper in the sediment following biogenic silica diagenesis (Ocean Drilling Program Publication Services, 2012; Deep Sea Drilling Project Reports and Publications, 2012; Varkouhi, 2018). A few of the study sites are located beneath the largest and most intense equatorial upwelling zones on the Earth (the equatorial eastern Pacific Sites 846, 847, 850, 1225, 1226, and 1256; Fig. 1). This matter is of particular

significance as the equatorial eastern rims of the North and South Pacific Ocean were some of the major depocentres of biogenic opal during the Middle Miocene to Early Pliocene (Ingle, 1980, 1981; Behl, 1999). In 39 of the selected borehole sites, pelagic biogenic opal is deposited with fine detrital sediments formed through chemical alteration of windblown volcanic ash (or volcanic glass) on the seabed, in addition to products of continental weathering processes from the source regions (i.e., siliceous oozes that are accompanied by clay, silt, and sometimes volcanic ash and tuff; according to Varkouhi and Wells, 2020). Though detrital-based, small proportions of marine calcareous nannofossils (sometimes benthic and planktonic foraminifers) are admixed with the diatomaceous sediments from these sites, with the peak proportion being for the Leg 167 of ODP, Sites 1016 and 1022 (15% of total sediment volume; Shipboard Scientific Party, 1997a, 1997b). For the remaining 28 carbonate-based sites, biosiliceous sediments, which may have small varying fractions of commonly fine-grained siliciclastic materials (their peak clastic content being ~10% for Site 1207; Shipboard Scientific Party, 2002), are deposited with calcareous nannofossil oozes (and foraminiferous). Whether clay-based or carbonate-dominated, the content and grain-size variations of siliciclastic serve as a proxy for assessing the degree of proximity to terrestrial sources for basinal biosiliceous deposits (e.g., Murray et al. 1992a, 1992b).

3. Data and methods

Initial reports, related sources, and publications for the ODP and DSDP boreholes involved in this research contain data regarding the dominant lithology recovered at

the sites, age, petrophysical properties, pore-water chemistry, mineralogy, thickness, and thermal information for the intervals of interest ($TZ_{A/CT}$ and its accommodating successions) (see Hein et al., 1978; Neagu, 2011; Ocean Drilling Program Publication Services, 2012; Deep Sea Drilling Project Reports and Publications, 2012; International Ocean Discovery Program, 2014). This information is compiled in Appendices I–III, and methods used to assess those parameters assembled in these tables are described in detail in the ODP technical notes (e.g., Mazzullo and Graham, 1988; Fisher and Becker, 1993; Blum, 1997). Below, our approach to constraining the depth to both frontiers (top and base) of the $TZ_{A/CT}$ penetrated by the studied borehole sites is explained. Also, with reference to the principal function of age and *in situ* temperature of drilled sediments for the framework of present study, the methodology of ODP for measuring these parameters is briefly described.

3.1. Identification of $TZ_{A/CT}$

3.1.1. Petrophysical properties

Due to their very small measurement intervals (e.g., 0.7–1.5 m for density stations and ~30 cm for the downhole logging tools, according to Blum, 1997; Varkouhi, 2018), petrophysical-property measurements are accurate indications of the depths to top and bottom of $TZ_{A/CT}$ (e.g., Compton, 1991; Nobes et al., 1992; Chaika and Williams, 2001; Neagu, 2011). In this study, the top and base of the $TZ_{A/CT}$ were principally tracked by following the approach of Neagu (2011), using the DSDP- and ODP-conducted physical-property assessments. While petrophysical data for ODP sites are well available, poor recovery of core samples limits the spectrum of

physical-properties measurements in DSDP sites. According to Neagu (2011), on density–depth profiles, for example, the top of $TZ_{A/CT}$ occurs where there is a great positive deflection of the bulk sediment density (Fig. 2). This is followed by a slight negative deflection near the base of $TZ_{A/CT}$ as observed on the sediment density curve (see Varkouhi, 2018; Varkouhi et al., 2020a, Varkouhi et al., 2020b). Such slight deflections can be related to the non-uniform nature of mineralogical transformation from biogenic to diagenetic opal, which acknowledges the presence of sediments with little or no precipitates of diagenetic opal at and near the base of the transition stratigraphically below the sediments with significant indications of opal-CT (Varkouhi et al., 2020b). This does not mean that the density decreases (or the porosity increases) in the preserved cores below the transition, but in fact its average value remains higher than that in the sediment box above the transition despite the deflections. Of course, the sediment box below the transition still exhibits marked porosities because the sediment is almost devoid of biogenic silica, while opal-CT precipitates in varying proportions which partly inhibits further anomalous compaction of the porous matrix (especially for clay-rich deposits) (Varkouhi et al., 2020a). In addition, the post-diagenetic characteristic of normal mechanical compaction of biosiliceous deposits helps maintain porosity (and therefore resists against large density increases) below the $TZ_{A/CT}$. The thickness of $TZ_{A/CT}$ can thus be estimated via the density profile from the depth of the marked positive gradient between two adjacent values within a specific lithologic interval to the point where the subsequent slight negative density deflection ends. The accuracy of density profile is further supported by combining this indicator with data of porosity profiles

which commonly mirror density values at comparable depths across the $TZ_{A/CT}$ and sonic velocity and resistivity increases as a results of density increase (after Varkouhi et al., 2020a). The consistency between qualitative identification of $TZ_{A/CT}$ based on physical-property variations and the highest quantitative gradient between two adjacent values within this depth interval suggests that Neagu's (2011) method is a credible means for characterising the top and bottom of $TZ_{A/CT}$, and quantifying the thickness of this reaction front (Varkouhi et al., 2020a).

In addition to petrophysical properties, for each investigated borehole site there are other data types, including the results of X-ray diffraction (XRD) analysis, smear slides, descriptive lithology, seismic reflection, and pore-water inorganic chemistry which were used to constrain the depth of the $TZ_{A/CT}$. These methods and their associated limitations for tracing the $TZ_{A/CT}$ are presented below.

3.1.2. Other diagnostic methods

— *XRD*

The XRD-detected appearance of diagenetic opal in sediments is mostly not coincident with the depth of the $TZ_{A/CT}$, i.e., the precipitates of opal-CT in opal-A-rich deposits above the petrophysical $TZ_{A/CT}$ have been previously documented (e.g., Nobes et al., 1992; Rice et al., 1995; Varkouhi et al., 2020b), making the recognition of $TZ_{A/CT}$ using XRD only a rough estimate. As a result, the XRD-defined boundary is a very large opal-A-rich $TZ_{A/CT}$, which is not in accord with the thin opal-CT-rich nature of the $TZ_{A/CT}$ as defined by former studies (Davies and Cartwright, 2002;

Neagu et al., 2010; Neagu, 2011; Varkouhi, 2018; Varkouhi et al., 2020a). With the exception of Leg 19 which details of XRD data are reported by Hein et al. (1978), no XRD analyses were performed on sediments of DSDP wells, but the results of this analysis in a wide range of sampling interval resolutions (from 1 to 30 m; after Varkouhi, 2018) are available for ODP sites. These data were used by the present study to identify the top of the $TZ_{A/CT}$ at the investigated sites as the first occurrence of opal-CT in the sediment. XRD is not a reliable indicator of opal-A presence in the sediment as it cannot detect the structure of starting non-crystalline silica during the early stage of diagenesis (Rice et al. 1995). Further, the XRD band of opal-A is overlapped by hk reflections that correspond to clay components (Singh and Gilkes 1993), making opal-A undetectable by XRD procedures (Varkouhi et al., 2020b).

— *Smear slides*

DSDP and ODP used smear slides to identify biogenic, lithogenic, and mineral components of sediments, among which biogenic opal has been given particular attention. These data were used by this study to represent rough indicators of the top of $TZ_{A/CT}$ as the depth where the relative abundance of solid biogenic silica, including diatoms, radiolarians, silicoflagellates, and sponge spicules in sediments, decreases sharply and dramatically. Smear slides define the base of $TZ_{A/CT}$ as the depth where opal-A disappears from the sediment, which is an imprecise estimation as the disappearance of biosilica can be linked to major lithological variations instead of transformation to opal-CT. The limitations associated with precision of the smear-slides analyses (e.g., Kinoshita et al., 2009), additionally the non-uniformity of

mineralogic transition from opal-A to opal-CT (Nobes et al., 1992; Varkouhi et al., 2020b) lead to the definition of a large $TZ_{A/CT}$. Smear slides are widely used for estimation of the proportion of biogenic opal in sediments. There have been discussions on how reliable the methods standing as alternatives for smear slides, including wet chemical analysis via the chosen leaching reactant determine the yields of biogenic silica dissolution, and thereby opal content of sediments (e.g., Olivarez Lyle and Lyle, 2002; Rahman et al., 2017; Pickering et al., 2020). These studies argue that the results of wet chemical analyses often highly underestimate the content of biogenic opal in sediment mixtures that smear slides still remain a more reliable approach to assess the relative abundance of opal.

— *Descriptive lithology*

Lithological description of cores provides an approximate identification of $TZ_{A/CT}$ top as the depth of the first appearance of porcellanite and/or chert layers in biosiliceous sediments (e.g., Behl and Garrison, 1994). As the leading opal porcellanite and chert (sometimes siliceous claystone) composition of sediment box hosting the $TZ_{A/CT}$ can continuously develop far below the depth of this boundary, commonly to the depth of transition from opal-CT to quartz, the base of the $TZ_{A/CT}$ cannot be easily determined. Lithological features roughly detect the base of $TZ_{A/CT}$ as the lowermost occurrence of opal-A (the final disappearance of opal-A) if no major changes in composition of the sediment below this boundary are observable. The base of $TZ_{A/CT}$ does not coincide with the uppermost occurrence of diagenetic quartz, which is at the depth of transition from opal-CT to quartz far below the $TZ_{A/CT}$.

— *Seismic reflection*

The sharp porosity reduction across the $TZ_{A/CT}$ can produce a high-amplitude reflector that is commonly recognised on seismic sections by a discordant geometry with host strata (Brekke, 2000; Davies, 2005; Ireland et al., 2010; Neagu et al., 2010). Due to its limited vertical extent, the $TZ_{A/CT}$ is however below or at the vertical resolution limit of the seismic data (Varkouhi et al., 2020b) that its thickness cannot be determined using this identification method.

— *Pore-water chemistry*

Depth profiles of dissolved silica and other major ions are reliable diagnostic tools for tracking the initiation of diagenetic opal precipitation. The onset of this process is in particular illustrated by dissolved silica sink which commonly coincides with the top of petrophysical $TZ_{A/CT}$ (Fig. 2), and considered to be a strong means of extracting the signatures of ongoing silica diagenesis (Varkouhi et al., 2020b). With the exception of DSDP Sites 387, 469, and 471 which details of pore-water analysis are reported by Hesse and Schacht (2011), the DSDP did not perform inorganic pore-water chemistry program. The results of this program exclusively focused on analyses of pore-water samples at different depths are also available for a limited number of ODP sites. This study used the silica concentration profiles to determine the depth to top of the $TZ_{A/CT}$ penetrated by the investigated boreholes as the zone, where the concentration suddenly drops. Silica profiles roughly define the base of $TZ_{A/CT}$ as the depth where concentration sink turns to the zone of gently decreasing concentrations with depth if high-resolution small sampling spacings are followed.

3.2. Temperature estimates

The procedure to estimate downhole temperatures of ODP- and DSDP-drilled sediments follows Fisher and Becker (1993). Two types of ODP tools are available for measuring the downhole temperatures: (1) the APC (advanced piston corer) and (2) the WSTP (water-sampling temperature probe). The tools are used separately to measure sediment temperature at different depths during a coring sequence.

The *in situ* temperatures at the ODP sites were measured using the APC tool designed to assess the sediment temperature as a piston core is taken (Appendix IV). The two steel prongs at the base of the APC tool case fit into the borehole at the bottom of the annular cell in the cutting shoe of the piston corer. The instrument is fixed in the annular cell with the help of the prongs. The resistance temperature apparatus contained in the prong is used to measure the sediment temperature. The wall thickness of the cutting shoe outside the annular cavity is about 1.5 cm, giving it a few minutes of time constant in the sediment. The APC was thus held in place for 15–20 minutes to obtain enough data for extrapolating the *in situ* temperature.

The temperature of the sediment of the analysed DSDP boreholes was measured using the WSTP tool (sometimes referred to as the Barnes/Uyeda probe) (Appendix IV). The WSTP, connected to the end of a core barrel, was lowered down the drill column and run on the coring line; thus requiring a break in coring (commonly 2 hours) to collect a fluid sample. The probe landed in the bottom-hole assembly, extending about 1 m into the sediment in front of the drill bit. As the fluid sample is

driven into a sample cell by the difference between hydrostatic and atmospheric pressures, only one sampling effort was possible during each extension (deployment). The fluid was pulled into the WSTP through a series of filters and mounted near the tip of the probe through the end of a sampling tube. The WSTP data logger continually sampled the resistance of the thermistors placed in the probe. The probe was then held in place for 15 minutes to gain enough data allowing for reliable extrapolation to the sediment temperature.

3.3. Age determination

Sediments hosting the $TZ_{A/CT}$ were dated using biostratigraphic evidence from diatoms, radiolarians, calcareous nannofossils, and planktonic foraminifera. Combining the biostratigraphic patterns of these different microfossils provides a well constrained chronology for nearly all of the studied borehole sites. Based on the zonation scheme of Okada and Bukry (1980), calcareous nannofossils were often used to develop the biostratigraphic framework of sequences. Due to notable contrasts in abundance above and below the $TZ_{A/CT}$, diatom assemblages were specifically used at sites where sufficient biosilica was contained in the sediment. Sediment ages determined by these methods are available through open access to the DSDP and ODP databanks. The present study has relied on the numerical ages provided by these sources, and the numerical stratigraphic ages of the deep-sea sediments for each ODP and/or DSDP site involved in this project have been derived directly from its respective ODP and/or DSDP initial report. In this case, each initial report has used a different version of the geological timescale.

4. Results

4.1. The $TZ_{A/CT}$

Characterisation of the depth to top and base of the $TZ_{A/CT}$ and its thickness for the ODP and DSDP sites included in this study using the diagnostic data types other than physical-property measurements is given in Appendix II, and in Figure 3 their results are compared with those obtained based on petrophysical depth profiles. For 18 out of 37 sites where silica transition could be determined using the XRD, this method estimated the depth to top of the transition within the opal-A sediment zone at sub-seabottom depths above the petrophysical $TZ_{A/CT}$ (Appendices I–II; Fig. 2). In 24 of the studied sites (almost 36% of the total 67 sites), the smear-slides measured the depth to surface of the transition zone at or very close to the depth of the petrophysical $TZ_{A/CT}$. For almost all (97%) of the studied sites where depths to both frontiers of the $TZ_{A/CT}$ were constrained using the smear-slides data, the $TZ_{A/CT}$ thickness was estimated thicker than that measured using physical-property changes (Appendix II). The lithologic data of sediments cored constrained the depth to top of the $TZ_{A/CT}$ for all the DSDP and ODP sites included in this study (Appendix II). Among the identification data types, the descriptive lithological analysis was the only method which approximated the depth to top of the transition zone for a peak number (~ 90%) of the studied boreholes very close to or coincident with the petrophysical $TZ_{A/CT}$ (Appendices I–II). For the studied sites where depths to both top and base of the $TZ_{A/CT}$ were determined using lithological data, the estimated thickness of this boundary was larger than that assessed using petrophysical features. Except for ODP Sites of Leg 127 and 128, where the $TZ_{A/CT}$ is almost clearly traced

on seismic profiles (Varkouhi, 2018; Varkouhi et al., 2020b), the depth of this boundary on low-quality seismic reflection data acquired for the DSDP and ODP sites used in this study was constrained with limited accuracy (Appendix II). In 27 out of 44 sites where the $TZ_{A/CT}$ was recognised on seismic profiles, the method estimated the depth of this boundary at or very close to depth of the petrophysical $TZ_{A/CT}$ (Appendices I–II). For most of the studied sites, limited resolution on acquisition and processing pore-water sampling intervals (being 10–30 m; after Varkouhi, 2018) did not allow for constraining the depth to bottom of the $TZ_{A/CT}$ and its thickness (Appendix II). In 40% of sites where the onset of silica diagenesis was detected from pore-water chemical profiles, the method estimated the top of the transition zone at or very close to the depth of the petrophysical $TZ_{A/CT}$. For the studied boreholes where the depth to both frontiers of the $TZ_{A/CT}$ was detected using silica concentration profiles, the boundary was far thicker than that measured using petrophysical data.

4.1.1. Overview of the characteristics of petrophysical $TZ_{A/CT}$

Because of limited availability and stratigraphic resolution of the other data sets presented above as compared with high precision of physical-property profiles and association of their abrupt and visible variations with the $TZ_{A/CT}$ (Fig. 2), the results discussed and concluded in this study are built on the characterisation of this boundary using the petrophysical contrasts between opal-A and opal-CT sediment units (Appendix I). The depth of the petrophysical $TZ_{A/CT}$ was generally 25 to 1050 meters below seafloor (mbsf), with the maximum sub-seafloor depth of 1050 mbsf

observed for the transition zones hosted by detrital-dominated sediments at the ODP Site 903 on the New Jersey continental slope (North America) and ODP Site 1150 from a deep-sea terrace of the Japan Trench. In detrital-rich basins, $TZ_{A/CT}$ depth varied mainly from 200 to 600 mbsf. In carbonate-dominated settings, the transition zone depth ranged chiefly from 150 to 500 mbsf (Appendix V). It was observed that the $TZ_{A/CT}$ thicknesses estimated using various down-core physical parameters are markedly lower than those measured based on the other data types described above (Fig. 3). Even for the lithological data which estimations of depth to top of the $TZ_{A/CT}$ for a majority of studied sites correlate with the petrophysical depths better than any other data types, the thicknesses measured using descriptive lithology are still far larger than the petrophysically determined thickness values (Appendices I–II). In compliance with Nobes et al. (1992) and Neagu (2011), the present work considers the maximum thickness, which is defined from minimum depth to top of the $TZ_{A/CT}$ determined by petrophysical data to maximum depth to base of this transition, as representative of the $TZ_{A/CT}$ thickness. The maximum thickness corroborates that the $TZ_{A/CT}$ is constrained between the point where a clear-cut petrophysical change starts and the point where the changes are indistinguishable from the natural background variability (Varkouhi et al., 2020a). Following Varkouhi et al. (2020a), due to dependence of porosity on water content loss as well as its high variability and sensitivity under biogenic silica diagenesis, the thickness values measured using porosity variations were used to closely represent the $TZ_{A/CT}$ thickness at the borehole sites assembled in this study (Appendix I). For all the studied ODP and DSDP sites $TZ_{A/CT}$ thickness was consistent across sites, ranging between 10 and 40

m with a mean value of ~23 m, despite having different dominant lithologies (statistics related to the $TZ_{A/CT}$ thickness for clay- and carbonate-dominated cases as well as statistics for all ODP and DSDP sites used in this study are presented in Appendix III). Almost 30% of transition zones were more than 25 m thick, regardless of the host lithology. Almost 80% of the clay-hosted transition zones and 60% of those hosted by carbonate-dominated lithologies were relatively narrow intervals having a thickness varying from 5< to 25 m (Appendix V). Remarkably, it was found that for both dominant host sediment types, i.e., clay versus carbonate, the modal value of $TZ_{A/CT}$ thickness fell within the 10–15 m range (Appendix V). The studied opal-A to opal-CT diagenetic transitions ranged in age from the Middle Palaeocene (Selandian) to the Late Pliocene (Piacenzian) (Appendix VI). The silica transitions found within mainly carbonate sediments had wider age ranges than transitions embedded in clay-rich sediments. The oldest (Middle Palaeocene) and the youngest (Late Pliocene) transitions appeared in carbonate-rich and clay-rich host lithologies, respectively. The most frequent silica diagenetic transition zones in clay-dominated and carbonate-rich sediment types were found to occur during the Late Miocene and Middle Miocene, respectively.

For all study sites, the age of the sediments in which the diagenetic transition was embedded was neither correlated with the thickness of the $TZ_{A/CT}$ nor with the opal-A content of the sediment (correlation coefficients being -0.02 and -0.46; Figs. 4A, B, respectively). However, when the sediment age was compared to thickness for carbonate-dominated sites, a weak correlation was observed ($r = 0.327$; Fig. 4A).

The present-day *in situ* temperature of the studied transition zones varies between 2 and 60 °C, with an average of ~25 °C (summary statistics for the $TZ_{A/CT}$ temperature values are presented in Appendix III). The maximum temperature, 60 °C, was recorded at the clay-hosted Site 1173 in the Nankai Trough, northwestern Pacific Ocean where the actual geothermal gradient is very high (170 °C/km; Appendix I). However, according to Neagu (2011), the 60 °C recorded at this site is not very reliable as it is estimated based on shallower temperature measurements that were extrapolated to the $TZ_{A/CT}$ depth. The lowest temperature (2 °C) was recorded at the carbonate-dominated Site 1090 near the Agulhas Ridge in the Southern Ocean where the geothermal gradient is anomalously low (8 °C/km; Appendix I). The temperatures at the depth of the transitions in clay-rich sediments ranged widely (~ 5–60 °C; Appendices I and VI), far more than for transitions hosted by carbonate lithologies. A modal value of 35–40 °C was observed for the study sites having the clay-dominated transitions. The frequency of carbonate-hosted transitions increased with higher temperatures, while there was no apparent relationship between frequency and temperature for clay-hosted sites (Appendix VI).

Regardless of the dominant lithology, the present-day $TZ_{A/CT}$ temperature was moderately correlated with $TZ_{A/CT}$ thickness ($r = 0.588$) (Fig. 5A). Clay-hosted $TZ_{A/CT}$ showed a much stronger relationship between $TZ_{A/CT}$ temperature and thickness ($r = 0.659$) than did carbonate-embedded transitions ($r = 0.424$). One of the most significant observations was that, under the present-day constant geothermal gradients reported, the temperature contrast between the top and bottom of the $TZ_{A/CT}$

itself was also correlated to the $TZ_{A/CT}$ thickness (Fig. 5B).

4.2. Temperature–age relationship

The relationship between *in situ* temperatures at the $TZ_{A/CT}$ and the age of the sediment hosting this diagenetic boundary followed the general trend previously shown by Hein et al. (1978) exhibiting an inverse correlation between these two variables (i.e., the older the diagenetic transition zone, the lower its measured temperature). Figure 6A follows the general trend of the temperature–age relationship presented by Hein et al. (1978), and exhibits an overall moderate inverse correlation between these two variables. However, a series of silica transitions younger than the Middle Miocene were almost evenly distributed across the 3–40 °C temperature range. Though the data points in Figure 6A generally have error bars representing the possible age range of the sediment, this inverse relationship remains statistically valid. When clay- and carbonate-dominated sites were assessed separately, the temperature and age data points were moderately anticorrelated for clayey sites, while only a weak inverse correlation between these variables was observed for carbonate sub-populations (Fig. 6B; correlation coefficient values being -0.5 and -0.15 for clay- and carbonate-dominated sites, respectively).

5. Discussion and implications

5.1. Controls on silica diagenesis

While available alkalinity and Mg are the most relevant factors for forming a magnesium hydroxide compound ($Mg(OH)_2$), which plays a key role in coagulation

and nucleation of opal-CT lepispheres (e.g., Williams and Crerar, 1985), burial temperature and age are considered to be fundamental controls on the overall opal-A to opal-CT transformation (e.g., Kuramoto et al., 1992; Hesse and Schacht, 2011). Marked dependence on temperature of th e precipitation rate of lepispheres is experimentally acknowledged by Kastner and Gieskes (1983) who indicated that the dissolved Mg decreases and the alkalinity is consumed as the $Mg(OH)_2$ continues to precipitate under increased temperatures. Although the early diagenetic (a few cm below the seabed) transformation of silica polymorphs is confirmed in some Palaeozoic and Mesozoic siliceous deposits independent of temperature and driven by the pore-water silica content (e.g., Zijlstra, 1994; Racki and Cordey, 2000; Migaszewski et al., 2006; Madsen et al., 2010; Jurkowska et al., 2019; Świerczewska-Gładysz, 2020a, b), formation of $TZ_{A/CT}$ requires conversion of opal-A to opal-CT mineral phase during later diagenesis on significant depths under the palaeogeothermal gradient (e.g., Iijima and Tada, 1981; Neagu, 2011; Pisciotto et al., 1992; Kuramoto et al., 1992; Weller and Behl, 2015; Varkouhi, 2018).

The specific surface area is another factor especially for the initiation of the reaction through exerting controls on the solubility of various biogenic silica. This factor thus intends to explain the direct impact of biogenic silica solubility differences due to varying surface areas of siliceous shells on the dissolution rate of opal-A and the pore-water saturation state with respect to silica polymorphs (Williams et al., 1985). The dissolution of opal-A can bring silica in pore waters to values approaching solubility level of disordered opal-CT as the reactive surface area of opal decreases

with further dissolution, and opal-CT enters the accumulation stage (Hinman, 1998).

The rate of opal-A to opal-CT transformation is also affected by the host lithology; implying that the precipitation rate of opal-CT is much higher in carbonate than in clay-hosted sediments. Predominance of opal-CT precipitation rate in carbonates is particularly governed by the dissolution of carbonate minerals which provides the necessary levels of alkalinity for increasing the total solubility of silica, and therefore the Mg for the formation of $Mg(OH)_2$ in the nuclei (Kastner et al., 1977). Under essentially all natural conditions, the activity of this positively charged hydroxyl complex provides nucleation sites for opal-CT lepispheres by attracting silanol groups (Iler, 1973; Williams and Crerar, 1985). In clay-dominated sediments, conversely, the detrital clayey materials stimulate formation of authigenic aluminosilicates which compete with the formation of diagenetic silica for the available alkalinity from the seawater, leading to their enrichment in Mg, and hence a reduction in precipitation rate of opal-CT from dissolved silica. These authigenic reactions, which are referred to as reverse weathering (Emerson and Hedges 2008; Loucaides et al. 2010), commonly occur concomitant with silica diagenetic transformation and often influence the solubility and chemical kinetics of dissolved silica (Varkouhi et al., 2020a). The reduced rate of biogenic silica diagenesis in clayey deposits is because the fine-grained aluminosilicate matter incorporated into or deposited on the surface lattice of biogenic silica frustules limits its solubility and reactivity by impeding covers (after Varkouhi and Wells, 2020). As shown in many studies (e.g., Lancelot, 1973; Van Cappellen and Qiu, 1997a, b; Michalopolous and

Aller, 2004; Tatzel et al., 2015; Ehlert et al., 2016; Rahman et al., 2016; Rahman et al., 2017; Bernhardt et al., 2020; Geilert et al., 2020), this process is carried out via adsorption of extraneous metallic cation species—they are mainly the constituents of clay minerals—especially Al and Fe from sediment pore waters onto the surface layers of opal, which influence its dissolution behaviour by reducing the solubility. It has however been argued that due to rather conservative nature of Al, the supply of this metal species for precipitation of authigenic clays and probably zeolites by decomposition of detrital aluminosilicates is a major problem of its mobility (Varkouhi et al., 2020a). Therefore, it is very unlikely that the formation of authigenic aluminosilicates when Al is present in the pore waters possesses the potential to cease the precipitation of opal-CT from dissolved silica.

As a factor partly triggering the opal-A to opal-CT conversion in the sediments below the seabed, degradation of organic matter (i.e., dissolved organic matter) accelerates the dissolution rates of amorphous silica via a complexation mechanism which increases the alkalinity, pH, Eh, and ammonia content of the pore water early in the diagenetic process (Bennett, 1991). Accordingly, the opal-A to opal-CT transformation rates reduce if organic compounds are preserved later in the diagenetic sequence (Hinman, 1990).

5.2. Controls on $TZ_{A/CT}$ thickness

As the rate of opal-A to opal-CT transformation is predominantly temperature dependent (e.g., Kastner and Gieskes, 1983), it can be inferred that temperature

599 exerts a major control on the upward advance and the thickness of the $TZ_{A/CT}$ as well.
600 This inference is supported by the studied transition zones being relatively narrow
601 intervals (maximum thickness = 40 m; Appendix I), regardless of the dominant host
602 sediment type, age, and/or biogenic silica content. According to Littke et al. (1991),
603 temperature is a first-order control on thickness where the $TZ_{A/CT}$ is relatively narrow.
604 The correlation observed between the $TZ_{A/CT}$ temperature and thickness values (Fig.
605 5A) further supports temperature being a primary control. A wide range of
606 differences in temperature between the top and bottom of the $TZ_{A/CT}$ (0.12–5.9 °C;
607 Appendix I) suggests that other diagenetic drivers, such as time, pore chemistry,
608 surface area, and host lithology (e.g., Williams et al., 1985) may partially affect the
609 $TZ_{A/CT}$ thickness. Temperature variability within the $TZ_{A/CT}$ may reflect variations in
610 the thermal regime of the host sediment (after Neagu, 2011), i.e., the higher the
611 temperature contrast over the $TZ_{A/CT}$, the higher the heat flow within the sediment
612 (and vice versa). As indicated in Figure 5B, the $TZ_{A/CT}$ intervals are distributed in
613 both low and high heat flow regimes.
614
615 The association of $TZ_{A/CT}$ thicknesses with high temperature contrasts agrees with the
616 observations of Littke et al. (1991) linking narrow intervals to areas marked by high
617 geothermal gradients. However, a group of the analysed narrow transition zones are
618 clustered around values having a minimal temperature difference (< 1 °C
619 temperature contrast; Fig. 5B). Littke et al. (1991) suggest that silica diagenesis
620 across some of these transition zones occurred when the geothermal gradient was
621 significantly higher than at present. Therefore, the temperature contrast through the

$TZ_{A/CT}$ would not be representative of the actual diagenetic temperature of opal-A to opal-CT transformation. This type of transition zone is discussed in the next section.

5.3. Revisiting the silica diagenesis stability field

The temperature–time relationship during later diagenetic silica formation has been studied extensively (e.g., Hein et al., 1978; Mizutani, 1977; Pisciotto, 1981a). Hein et al. (1978) were the first to propose a diagenetic stability field necessary for initiation of opal-A to opal-CT transformation. They estimated the age and present-day temperatures at opal-CT formation depth for siliceous marine deposits from the southern Bering Sea, the Monterey Formation, and some North Pacific chert and porcellanite sediments. Their stability field was based on the strong negative correlation of time and temperature during the ongoing precipitation of opal-CT (i.e., active diagenetic processes) and included the upper and lower boundaries of diagenetic silica formation (see Fig. 6B). According to Hein et al. (1978), early silicification (formation of opal-CT) takes place at relatively deep burial depths (> 500 mbsf) and moderate temperatures (35–55 °C) within 10 m.y., while more than 30 m.y. is required for opal-A to opal-CT transformation at shallow burial depths (< 300 mbsf) and low temperatures (< 30 °C) (Fig. 6B).

Our negatively correlated age and temperature data points fit poorly within the Hein et al. (1978) time–temperature field (Fig. 6B). Our data match the lower boundary of the stability domain slightly better than the upper boundary. The low temperature (< 30 °C) data points, however, are located mostly outside the original lower boundary.

We postulate that this non-conformity is because the Hein et al. (1978) time–temperature relationship field was based on limited data. As the initial diagram was based on only six data points, it needs to be extended for use in constraining the temperature–time stability realm of diagenetic silica. This section therefore aims to extend the time–temperature stability field of opal-CT, which greatly helps determine the present diagenetic state of the $TZ_{A/CT}$ and has implications for thermal history of sediments undergoing biogenic silica diagenesis. Below our approach to revise the stability diagram is discussed.

5.3.1. Expansion of Hein et al.' (1978) diagram

The approach taken here is to expand the Hein et al.' (1978) diagram by including the age and temperatures of a set of $TZ_{A/CT}$ intervals that we believe are diagenetically the most plausible active candidates (those zones across which biogenic silica diagenesis is still occurring). Due to lack of uplift and erosion, the sedimentary columns hosting the active transitions are presently at their maximum burial depth, and the onset of silica diagenesis at these sites is not concurrent with unconformities. As such, the ongoing precipitation of opal-CT is thus related to the present-day burial depth. Therefore, the age and present-day temperature at the depth of an active $TZ_{A/CT}$ can roughly represent the time and temperature when formation of opal-CT across the $TZ_{A/CT}$ was first initiated. This assumption is possible as the active transitions represent modern isothermal features that are in near equilibrium with the present-day geothermal gradients (after Pisciotto et al., 1992; also see Varkouhi, 2018).

The likely active $TZ_{A/CT}$ intervals and the criteria used to select these intervals are listed in Table 1. Seismic identification criteria were not used as, due to their low quality, the $TZ_{A/CT}$ is often difficult to identify from DSDP and ODP seismic profiles. Only a limited number of the investigated transition zones (21 sites) were considered to be presently active (Table 1). These likely active boundaries were found in continuous stratigraphic sections where there are no major breaks or unconformities in sedimentation. These transitions are found in young sediments (Middle Miocene and younger) marked by high thermal gradients and generally containing sufficient amounts of biogenic silica. Moreover, the concentration of silicic acid sharply decreases across the active transitions (e.g., Varkouhi, 2018; Fig. 2). According to thermodynamic analyses conducted by Varkouhi (2018) and Varkouhi et al. (2020b), the correspondence between the dissolved silica removal from the interstitial water and distribution of opal-CT at the depth of this boundary implies that the present-day sink for silica across the $TZ_{A/CT}$ is due to the ongoing precipitation of diagenetic opal. The proposed stability field is defined mainly on the time–temperature data from likely active transitions and represents an expanded version of the Hein et al. (1978) diagram (Fig. 7A).

Among the active sites used for extending the Hein et al. (1978) diagram, Site 1173 has the highest ODP-reported $TZ_{A/CT}$ temperature (60 °C). However, according to Neagu (2011), the ODP-recorded temperature for the transition zone at this site cannot be fully trusted as it has been calculated based on shallower temperature measurements that were extrapolated to the $TZ_{A/CT}$ depth using an anomalous

691 geothermal gradient of 170 °C/km estimated for the upper 300 m. It is acknowledged
692 that deeper than 300 mbsf at Site 1173 thermal conductivities have increased by 10%
693 (from 1.05 to 1.16 W/m °C; after Shipboard Scientific Party, 2001b), so the thermal
694 gradient should decrease proportionally (from 170 to 155.5 °C/km, given a reported
695 heat flow of 0.18 W/m^2 or 180 mW/m^2 for this site; Appendix I), and the $TZ_{A/CT}$
696 temperature (55 °C) is therefore somewhat lower than that reported by the ODP
697 (Appendix I). These very high thermal gradients have been explained by geological
698 and geophysical studies of the ocean bottom around the Nankai Trough near the
699 drilled off Site 1173, revealing that the northern edge of the very hot Philippine Sea
700 Plate is subducting underneath the Japanese landmass along this trough (Moore and
701 Karig, 1976; Kinoshita and Yamano, 1986). As the heat flow in the northern edge of
702 the plate offshore of the Nankai Trough is highly scattered (0.02–0.2 W/m^2), hot
703 parts of the Philippine Sea Plate are showing up around the trough area (after
704 Kinoshita and Yamano, 1986). Magnetostratigraphy shows that the age of the
705 sediment accommodating the $TZ_{A/CT}$ has been slightly overestimated (~0.2 m.y.)
706 using the ODP biostratigraphic data (i.e., the biostratigraphic age being 3.5 m.y.;
707 Shipboard Scientific Party, 2001b). Accordingly, the slightly modified temperature
708 and age of the $TZ_{A/CT}$ at Site 1173 (55 °C and the magnetostratigraphic age of 3.3
709 m.y., respectively; Fig. 7A) were used to fit the upper boundary of the stability field.
710
711 Insufficient time to reach an equilibrium temperature while drilling as well as the
712 temperature estimation based on shallower temperatures extrapolated to the $TZ_{A/CT}$
713 depth (Shipboard Scientific Party, 1981) are the two major sources that have affected

the DSDP-reported $TZ_{A/CT}$ temperature value in Site 471. The DSDP underestimation of the $TZ_{A/CT}$ temperature at this site (22.5 °C; Appendix I) is because small variations in the thermal conductivity of opal-CT-rich sediments below the $TZ_{A/CT}$ (up to 4%; following Shipboard Scientific Party, 1981) have not been involved in assessment of the geothermal gradient. The $TZ_{A/CT}$ temperature was therefore shifted to 23.5 °C (Fig. 7A), using a modified thermal gradient of 138.5 °C/km, which fits the lower boundary of our extended stability field.

Also, some uncertainties in constraining the $TZ_{A/CT}$ depth have led to slightly underestimated and overestimated $TZ_{A/CT}$ temperatures at Sites 184 and 1172, respectively (Hein et al., 1978; Shipboard Scientific Party, 2001a). The $TZ_{A/CT}$ temperatures for Sites 184 and 1172 were thus modified, and placed very close to and fitting the upper boundary of the revised opal-CT stability field, respectively. The $TZ_{A/CT}$ temperature at Site 184 (51.2 °C; Appendix I) was corrected to 52 °C (Fig. 7A) using modifying the DSDP-reported 600 mbsf the depth of this boundary (Shipboard Scientific Party, 1973; Hein et al., 1978) to 610 mbsf. Likewise, in Site 1172, the depth of the transition (500 mbsf; as reported by Shipboard Scientific Party, 2001a; Appendix I) was modified to ~450 mbsf, which resulted in a temperature reduction of 2.4 °C (from 25.7 to 23.3 °C; Fig. 7A).

This extended diagram follows the general trend of a progressive and ongoing transformation from opal-A to opal-CT, implying the negative correlation between temperature and time, valid for all diagenetic processes (after Giles, 1997). Since the

data points from active transitions cover only the younger age zone of the extended stability field (< 13 m.y.; Middle Miocene onwards), the boundaries of this diagram were extrapolated to older ages (from the Middle Miocene to Middle Eocene) using the age–temperature data from some of diagenetic transformation boundaries that do not meet the applicable recognition criteria for active transition zones (see Table 1 and Varkouhi et al., 2020b), but fit the inverse correlation pattern of temperature and age established for ongoing silica diagenetic reactions (transition zones with uncertain diagenetic status, shown by labelled red triangles in Fig. 7A). These data points (red triangles in Fig. 7A) were chosen for the extrapolation of the stability field to > 13 m.y. rather than any of the others shown in Figure 7B because:

1) these data points persist following the trend of temperature–time relationship observed for the younger part of the stability field better than others.
2) low temperature nature of these old transitions (Early Miocene and older) shows it is very unlikely that these boundaries to be presently arrested (according to Neagu, 2011 and literature there in).
3) trend of temperature evolution in time among these data points shows a nearly consistent variability pattern, with the least deviation from parallelism to the initial stability field.

5.3.2. Revised versus initial stability field

Given its narrower temperature range, the Hein et al. (1978) stability field is captured within our opal-A to opal-CT age–temperature stability field. Comparable to the

transition zones studied by Hein et al. (1978), the transitions from this study are mostly ranged in age from the Middle Eocene to Late Pliocene; the time range for the extended stability field was therefore defined the same as that of Hein et al. (1978) diagram. According to the extended stability field, transformation of opal-A to opal-CT under shallow-burial conditions at low temperatures (< 30 °C) takes more than 35 m.y. (Fig. 7A). This is in broad agreement with Hein et al. (1978). They claim that the silicification reaction, under the constraints of a shallow burial depth and low temperatures, depends mainly on time. However, an increase in the rate of silica diagenesis relative to the sedimentation rate would still be needed to sustain the active transformation of opal-A to opal-CT following the initial opal-CT precipitation. The increasing rate of sedimentation with time governs the upward migration of geochemical zones, causing the favourable conditions for opal-A to opal-CT transformation no longer sustained (Clayton, 1984; Zijlistra, 1994; Jurkowska et al., 2019). Thus, time cannot be the first-order control for increasing the reaction rate. Therefore, even at low temperature conditions, the opal-A to opal-CT reaction has been primarily caused by temperature, of course partly influenced by other agents such as sediment age, lithological factors, and the role of dissolved Mg, alkalinity, and degradation of organic matter which induce changes in the chemistry of sediment pore water.

It should be noted that the unusual accumulations of young (0.4–4 m.y.) opal-CT porcellanites and cherts at very low surface temperatures commonly between 0 and 4 °C in near-seabed sediments (e.g., Bohrmann et al., 1990; Botz and Bohrmann,

1991) is in contrast with the established models of later diagenetic precipitation of opal-CT in deep-sea deposits, which require the dominance of higher transformation temperatures (from 18 to 56 °C; Pisciotto, 1981a). Moreover, the inverse correlation between age and formation temperature of opal-CT, implying silica transformation at higher temperatures in young deposits challenges very low surface temperatures being a major control on opal-CT precipitation near the seabed (Varkouhi and Wells, 2020). The analysis of near-seabed opal transformation at very low temperatures was, however, not undertaken in this study as silica transformation reaction diagnosed in the surface sediment does not represent an opal-A to opal-CT transition zone, and the diatom ooze persists well below this horizon, e.g., to a penetration depth of 166.2 mbsf at the ODP Site 751 from the Antarctic, according to Botz and Bohrmann (1991) and Varkouhi and Wells (2020).

Based on the revised stability field, the active precipitation of opal-CT at moderate temperatures (ranging from 35 to 55 °C) under shallow burial settings takes place within a 3 m.y. period, a much shorter period than the transformation time estimated by the Hein et al. (1978) diagram for moderate temperature conditions. The extended diagram shows that at high temperatures (> 55 °C), the transformation will likely occur rapidly (< 1–2 m.y.) regardless of burial depth. Thus, an earlier transformation occurs at higher temperatures.

5.3.3. Diagenetic state of $TZ_{A/CT}$— Remarks and implications

To confirm that the negative temperature–age relationship illustrated by the extended

opal-CT stability diagram adequately describes the study data, time and temperature values for the $TZ_{A/CT}$ depths of the study sites were replotted on the extended diagram (Fig. 7B). Although showing a better fit to the lower boundary of the extended stability field than to the upper boundary, these data points (red triangles in Fig. 7B) do not fit the stability field. In general, these data do not follow the trend of decreasing temperature with age (and vice versa) under ongoing silica diagenesis.

Due to the limited availability of thermal and geochemical data, the current diagenetic status of the $TZ_{A/CT}$ at these sites is not known. It should be noted that a significant fraction of these data points (red triangles) fall outside the stability zone of active opal-CT precipitation, more explicitly below the lower boundary of the temperature–time field. The temperature and age of some of these sites are certainly not representative of an active opal-A to opal-CT diagenetic process (after Neagu, 2011). The $TZ_{A/CT}$ at these boreholes is characterised by low temperatures (< 20 °C) and is found in young sediments (Middle Miocene and younger; circled data points in Fig. 7B). According to Neagu (2011), such opal-A to opal-CT transitions having present-day low temperatures and younger ages likely represent regionally arrested features. Although there are no published supporting data, it seems that the arrest of the upward migration of $TZ_{A/CT}$ at these sites occurred due to a remarkable drop in the palaeogeothermal regimes that are possibly associated with past events of increased heat flow (Neagu et al., 2010). This argumentation assumes the thermal gradient has significantly decreased since the time of arrest (Davies and Cartwright, 2002) and that the magnitude of palaeogeothermal gradients was markedly higher

than the present at the burial depth of these arrested transition zones.

Davies and Cartwright (2002) explain how significant decreases in palaeogeothermal gradients and a cooling to modern values have possibly led to arrest of biogenic silica diagenesis by presenting arguments for an arrested transition zone from the Faeroe-Shetland Channel, northeast Atlantic margin. Based on constraints of overburden thickness accumulated during the Late Miocene and Early Pliocene, seabed temperature, and present-day geothermal gradient (38 °C/km), Davies and Cartwright (2002) calculate that a minimum thermal gradient of 60 °C/km would have been required to initiate active diagenetic transitions during the Middle and Late Miocene. Given the present temperature of this boundary (24 °C), a minimum 60 °C/km palaeothermal gradient would have been necessary to raise the palaeotemperature of the transition above 24 °C. This inference also incorporates a palaeoseafloor temperature of 5 °C during the initiation of silica diagenesis; a postulation that leads to an elevated palaeotemperature for the transition (29 °C at 400 mbsf), higher than that of its present-day depth (24 °C at 700 mbsf), when the boundary was closer to the seafloor. From this, Davies and Cartwright (2002) conclude that the opal-A to opal-CT transition might have been warmer early in deposition, and then much colder later in its history when arrest of biogenic silica diagenesis occurred, possibly due to sudden decreases in the extreme palaeothermal gradient. However, up to the present no supportive thermochronological evidence is available to support this.

The idea of an elevated palaeogeothermal when the transformation from opal-A to opal-CT initiated also explains why particular arrested sites exhibit young transition zones. The long established view of the development of an active silica diagenetic transition (prior to the arrest) originates from the theoretically based reasoning that temperature was the principal rate-controlling factor for growth and up-section migration of the transition through biosiliceous sediments (e.g., Kastner et al., 1977; Meadows and Davies, 2007; Neagu et al., 2010). This reasoning supports the assumption that the rate of transformation from biogenic to diagenetic silica prior to arrest has been fundamentally controlled by the palaeogeothermal gradients and thereby the palaeotemperatures. From this, we can conclude that the exceptionally elevated palaeogeothermal gradients have favoured rapid (high rate) transformation of opal-A to opal-CT, and therefore earlier formation of silica diagenetic boundaries (young high-temperature active transition zones). According to Hein et al. (1978) and Neagu et al. (2010), an active transition could also occur in an older and colder environment (i.e., slower rates of opal-A to opal-CT transformation) where thermal structure of the basin hosting silica diagenesis was not significantly disturbed in the recent past. The young low-temperature transitions with a currently arrested feature are however outside the realm of inverse age–temperature relationships for active diagenesis. These post-mid-Miocene boundaries, basically formed under elevated thermal gradients in the recent past, cooled quickly and were arrested at a regional scale possibly due to a sudden fall in geothermal fluxes of their host sediment.

It should also be mentioned that there have been discussions on the presence of Al

metal species with the potential impact on solubility and formation of authigenic clays as other explanation for the deviation of the young transition zones with likely arrested features from the calculated stability field (after Varkouhi et al., 2020a). The limited mobility of this metal cation due to its conservative behaviour additionally the non-uniform formation of diagenetic aluminosilicates however disaccord with the possibility that such authigenic precipitates can lead to cessation of the upward migration of the $TZ_{A/CT}$. This argument is further acknowledged by the fact that the extended stability field rules out the likely arrested transitions regardless of whether their dominant host sediment type is clayey or carbonate (circled data points in Fig. 7B). Accordingly, half of the young low-temperature transitions deviating from lower boundary of the extended stability field are accommodated in carbonate-rich deposits, which are devoid of fine detrital aluminosilicates to precipitate authigenic clays.

It is noteworthy to mention that the opal-A to opal-CT transition zones are developed in many continental margin depositional basins worldwide and according to many studies in the past three decades (e.g., Roaldset and He, 1995; Brekke, 2000; Davies and Cartwright, 2002; Berndt et al., 2004; Neagu et al., 2010), the $TZ_{A/CT}$ is not presently related to an active diagenetic reaction but is in fact arrested in its current position. However, most of the transition zones from different geographic regions are apparently bottom-simulating reflectors; in such situations the $TZ_{A/CT}$ is commonly concordant with the host strata and it is extremely difficult to make a case that the upward advance of $TZ_{A/CT}$ is arrested at all (as evident from Neagu et al., 2010).

Nevertheless, where the $TZ_{A/CT}$ cross-cuts stratigraphy or it is deformed contemporaneous with its arrest (in highly structured tectonic settings where local variations in heat flow and thermal conductivity result in a complex shallow thermal structure, according to Meadows and Davies, 2007, 2010; Neagu et al., 2010), the nature of arrested diagenesis can be determined.

5.4. Geothermal history of silica diagenesis

Mizutani (1970, 1971) proposed that the silica mineral phases of siliceous deposits are controlled by the thermal history experienced by the deposits during silica diagenesis. Accordingly, the location and temperature of the $TZ_{A/CT}$ primarily depends on the integrated geothermal history of the layer in which the transition zone is presently found (Tada, 1991; Langseth and Tamaki, 1992).

Amorphous silica has been transformed to opal-CT at all the studied ODP and DSDP sites. However, the $TZ_{A/CT}$ occurred at different depths in host sediments that ranged in age and temperature (e.g., Appendix VI). To further examine temperature variations in these sediments over time, the thermal history was estimated by multiplying the geothermal gradient and sedimentation rate ($G \times \omega$; as suggested by Mizutani, 1970) at the $TZ_{A/CT}$ depth and the results were plotted versus the age of the transition zone (Fig. 8). The accuracy of the temperature history values for those DSDP and ODP sites plotted in Figure 8 depends strongly on to what degree the variables (G and ω) can be estimated. We have used the gradients measured by the DSDP and ODP and the sedimentary histories were estimated based on the

magnetostratigraphic and biostratigraphic datum levels recognised at each site (available through the DSDP and ODP initial reports) that have been modelled versus sub-seabottom depth (e.g., Figure 30 in Shipboard Scientific Party, 1990a). The inverse relationship between the age and temperature history is represented by the power function (Fig. 8; correlation coefficient = -0.714). This pattern agrees with the age and temperature history relationships observed for the siliceous sediments by Pisciotto (1981b) who suggested that higher geothermal gradients in sediments with higher burial rates can account for the increased rates of opal-A to opal-CT transformation. Thus, high rates of silica diagenetic transformation correspond to high geothermal gradients and high sedimentation rates.

This study proposes a pattern of opal-A to opal-CT transformation that has active silica diagenesis at higher temperature gradients and higher sedimentation rates in younger sediments (Middle Miocene and younger), while silica transformation in sediments having low thermal gradients and low burial rates, corresponding to lower temperature history values, requires a much longer period of time (starting in sediments of Early Miocene age or older). Although the sediments with low thermal history still existed during the Early Miocene, their accommodated transition zones did not accelerate. It should be that the older sediments felt the same high heat flow as that the younger sediments experienced throughout the Miocene, but have presently arrested silica fronts due to an abrupt fall in the heat flux that promoted silica transitions. In contrast, it is also possible that the diagenetic reaction would not cease across these old transitions, and there has instead been a significant decrease in

944 the rate of silica diagenesis in the final stage of basin evolution so that the boundary
945 spared the rapid silica transformation (Meadows and Davies, 2007). As indicated in
946 Figures 7A, B, some of these low-temperature transitions fit the inverse temperature–
947 time relationships in silica diagenesis; likely implying a slower transformation rate
948 over the Early Miocene and older reaction fronts. However, due to the limited quality
949 and availability of seismic data for the offshore sites involved in this study, it is
950 presently not possible to determine the diagenetic state of these ancient cold reaction
951 boundaries. These patterns are best illustrated by the power function showing a near
952 steady upward trend when the $TZ_{A/CT}$ is found in younger sediments (a temperature
953 history > 4 °C/m.y.; Fig. 8), and a nearly constant trend in older sediments (a
954 temperature history < 1 °C/m.y.). Some of the transition zones characterised by a low
955 temperature evolution and a young age (younger than 14 m.y.) that do not fit this
956 opposing pattern of temperature and time can be characterised as likely arrested
957 candidates (circled data points in Fig. 8; also see Fig. 7B). Although the present-day
958 temperatures of the young arrested $TZ_{A/CT}$ are low (Fig. 7B), it is supposed that the
959 palaeogeothermal gradients of the sediment in which these transitions are contained
960 were significantly higher than the present-day gradients (e.g., Davies and Cartwright,
961 2002). This supports the view that the rate of biogenic silica diagenesis prior to arrest
962 was basically controlled by the palaeotemperatures, and that these palaeogeothermal
963 gradients caused a rapid transformation from opal-A to opal-CT (note that the
964 transformation occurred within young sediments at that time).
965
966 *5.4.1. ODP Sites 794 and 795*

— *Reconstruction of thermal history*

Given that silica diagenesis continues, over time, to advance upward over the active $TZ_{A/CT}$ and that increasing burial depth leads to higher temperatures (Langseth and Tamaki, 1992), a main control of this process must be related to the host sediment temperature history. Reconstructing the thermal history of host sediments, on a case by case basis, can provide further evidence to support this idea.

This section focuses on the thermal history of the sediments in the Sea of Japan, recovered by ODP 794 and 795, where the depositional sections display a full spectrum of siliceous lithologies and silica minerals (Shipboard Scientific Party, 1990a, b) and where the thermodynamic analyses suggest an active $TZ_{A/CT}$ in these biosiliceous deposits (Varkouhi, 2018; Varkouhi et al., 2020b). Stratigraphic correlation of abrupt petrophysical changes at these sites with the depth of lithological variations from highly porous diatom oozes to less porous porcellanites/cherts, the silica concentration sink, and the fall in opal-A content support this fact that the depth of the $TZ_{A/CT}$ is well constrained using physical-property contrasts (Fig. 9). The coincidence of dissolved silica depression very close to the petrophysical $TZ_{A/CT}$ with the depth where the pore water has reached a solubility equilibrium with opal-CT shows that silica is still being removed from the pore water and diagenetic silica is precipitating at this boundary (Varkouhi et al., 2020b). These boreholes represent a relatively uncomplicated natural laboratory to investigate the relation between temperature and time during silica diagenesis. It requires that the accumulation of siliceous sediments be nearly continuous with little

or no removal of sediment overburden (Fig. 9; Varkouhi, 2018; Varkouhi et al., 2020b); the $TZ_{A/CT}$ and its host sediments are thus currently at their maximum burial depth. As such, the present-day thermal gradient and the sediment accumulation rates under which silica diagenesis occurs can be used to reconstruct the thermal history. This reconstruction relied on the approach of Mizutani (1970).

The most striking aspect of this reconstruction is the rapid acceleration of the thermal history during Late Miocene in response to the peak rates of sedimentation in the biosiliceous interval above the active $TZ_{A/CT}$ at Site 794 (Fig. 10). In comparison, at Site 795 the temperature history values for the opal-A sediment above and across the $TZ_{A/CT}$ are higher than for Site 794, but are still in agreement with the high accumulation rates. The consistently higher rates of sedimentation at Site 795 from the Late Miocene to Recent coupled with a higher thermal gradient—relative to the sedimentation rates and geothermal gradient at Site 794—resulted in a greater burial temperature for sediment above the $TZ_{A/CT}$. Thus, at Site 795 maximum diagenetic silica concentrations occurred ca. 5 m.y. after deposition, whereas at Site 794 opal-CT reached a peak concentration only after ca. 8 m.y. post-deposition (Fig. 10).

Although it is noted that minor amounts of opal-CT were precipitated in the opal-A interval well above the $TZ_{A/CT}$, the maximum concentrations occurred only within the $TZ_{A/CT}$ (see Varkouhi, 2018 and Varkouhi et al., 2020b for a comprehensive review). Notably, this statement may reveal an issue given that our study considers the stability realm of opal-CT after this point, the petrophysical $TZ_{A/CT}$. Even though

minor contents of opal-CT precipitated before this boundary indicate the initiation of silica diagenesis chemical reaction, it does not become expressed in terms of abrupt physical-property changes until the reaction moves toward completion through in situ significant removal of biogenic opal and continuous extensive reprecipitation of diagenetic opal (Varkouhi et al., 2020a). Accordingly, these marked variations in sediment petrophysics (especially, the porosity drop) first occur where the $TZ_{A/CT}$ physically appears in the sediment as a distinct cored layer, which is coincident with the stability field of opal-CT where the kinetic of its precipitation dominates.

— *Modelling of silica diagenesis*

The transformation of biogenic to diagenetic silica is the dynamic process of re-establishing equilibrium with increasing temperature and time in a continuously changing biosiliceous medium (Curtis, 1977; Littke et al., 1991; Kuramoto et al., 1992; Worden and Burley, 2003). The thermodynamic modelling of this transformation reaction is therefore significant for tracking the evolution of silica phase-change process and temperature over time in sediment record and for further constraining the thermal history of the basin hosting silica diagenesis. The Arrhenius equation and the first-order reaction rate law (Appendix VII) were used to predict the transformation in the sediments at the representative Sites 794 and 795. The values chosen for the key parameters in the Arrhenius equation seem reasonable as increased transformation rates are associated with higher temperatures (Appendix VII; Fig. 11), a pattern that has been formerly documented (Pisciotto, 1981a, b; Dralus et al., 2015; Varkouhi and Wells, 2020). The model predictions of variability

of transformation ratios with temperature (Fig. 12A) closely mimics the previously documented variabilities versus temperature (e.g., Dralus et al., 2015; Wrona et al., 2017). The transformations temperatures also vary in the range of those established by silica diagenesis phase diagrams defined by Hein et al. (1978) (Fig. 12B).

The match between the modelled and observed opal-A to opal-CT transformation ratios, especially for the sediment overlying the $TZ_{A/CT}$ (i.e., the zone of low transformation ratios) in Sites 794 and 795 further validates this approach (Figs. 12C, D). The deviation the observed ratios take from the modelled values at high transformation ratios (i.e., from the depth of $TZ_{A/CT}$ downwards) is because the sharp reduction in opal content has directly impacted the relative amount of produced opal-CT, i.e., a sudden rise in the observed transformation ratios across this boundary by following the equation: $TR_{A/CT}$ = opal-CT/(opal-CT + opal-A), where $TR_{A/CT}$ is the observed transformation ratio of opal-A to opal-CT and the term opal-CT + opal-A represents the initial amount of biosilica.

An important result is the precision of the transformation ratio model for predicting the temperature at the present depth of the $TZ_{A/CT}$. The model slightly underpredicted the $TZ_{A/CT}$ temperature at Site 794, being ~37 °C at 293.5 mbsf (the ODP-measured value at the comparable depth is 37.5 °C; Appendix I), while precisely predicting the temperature for Site 795 (ODP estimate of 43.2 °C at 326 mbsf). At Site 794, the model predicts opal-CT began precipitating in the siliceous facies above the $TZ_{A/CT}$ with almost 16% (corresponding to the transformation ratio of 0.16, Fig. 12A) of

opal-A converted into opal-CT before reaching the $TZ_{A/CT}$. At Site 795, the value was somewhat higher (22%). The low transformation ratios in the opal-A sediment for both sites are due to low transformation rates of biogenic silica in this zone, where the burial heating is lower than that in the opal-CT zone (the $TZ_{A/CT}$ and the interval below). Though both values are low, the transformation rate above the $TZ_{A/CT}$ at Site 795 (being ~ 0.05/m.y.) is more than double that of the $TZ_{A/CT}$ at Site 794.

At a greater depth, a significant increase in the reaction rate in the opal-CT zone under increased burial heating caused ~75% progress in the transformation at Site 795, while the rate increase in the comparable interval from Site 794 promoted the transformation ratio to about 0.63 (~45% progress) (Figs. 11 and 12A). The marked warmer thermal history of opal-CT zone in Site 795 as compared to that of Site 794 accounts for a significant contrast between their amounts of reacted opal-A in this zone. Although the peak levels of opal-CT occurred at the $TZ_{A/CT}$ 8 and 5.3 m.y. following the deposition of biosilica at Sites 794 and 795, respectively (Varkouhi, 2018), the transformation of opal-A to opal-CT was not fully complete until 14 m.y. for Site 794 and 9.5 m.y. for Site 795 after initial deposition (Fig. 13). The strong correlation for opal-CT formation between temperature (burial depth) and age (Fig. 13) also suggests that thermal burial (present temperature) and sediment accumulation rates are principal controls of the transformation of opal-A to opal-CT.

6. Conclusions

Based on an exploration of the ODP and DSDP database, 67 globally distributed

offshore sites having an opal-A to opal-CT transition zone within Palaeocene- to Pliocene-aged sediments, were selected and examined for temperature–time relationships during biogenic silica diagenesis. The transition zone at these sites represents a narrow depth interval (up to 40 m in thickness) across which opal-A is transformed into opal-CT. Given the much higher resolution on acquisition and processing physical-properties sampling spacings as compared with other data types, this boundary was recognised in down-core profiles by its association with dramatic petrophysical variations in the host sediment. Regardless of the dominant lithology in which the transition zone was found (clay- or carbonate-rich sediments), the observation that all transition zones were relatively narrow and that their thickness was correlated to present-day temperatures suggest that temperature is the leading control on the thickness of these diagenetic boundaries.

Through this work, we used data mined from the ODP and DSDP programmes to extend the temperature–time stability field of Hein et al. (1978) used for the initiation of opal-CT formation. This new diagenetic opal stability field is an extension of the original diagram, updated by adding the age and temperature data of the active transition zones and transitions with uncertain diagenetic status fitting the inverse temperature–age correlation determined in this study. The extended stability field follows the widely accepted pattern of temperature variability over time for biogenic silica progressive diagenesis, implying an inverse relationship between temperature and time, valid for all diagenetic processes. According to the extended stability field, ongoing silica diagenesis under shallow burial occurs over 35 m.y. at

low temperatures (< 30 °C), within 3 m.y. at moderate temperatures (35–55 °C), and rapidly, regardless of the burial depth, at higher temperatures (> 55 °C). However, most data points from this study do not fit the extended stability field. The transition zones at some of these borehole sites, characterised by very low temperatures and captured in young sediments (Middle Miocene or younger), are likely to represent currently arrested features.

The thermal history is a principal control on the rates at which the silica diagenetic transformations occur. The geothermal history is primarily a function of sediment accumulation and thermal gradient. The analysis of thermal history for the studied sites suggests silica diagenesis occurs at high temperature gradients and high sedimentation rates in younger sediments (Middle Miocene and younger), while occurring over a longer time (Early Miocene and older) in sediments having low thermal gradients and lower rates of burial. Reconstruction of the temperature history of two representative wells having active transitions, ODP Sites 794 and 795, indicated that an accelerated thermal history during the Late Miocene and later occurred in response to the peak sedimentation rates in the opal-A interval overlying the transition zone. Compared to Site 794, Site 795 had higher accumulation rates from the Late Miocene to Recent and a higher thermal gradient that resulted in a greater burial temperature for the opal-A sediment unit, leading to an earlier onset of the diagenetic transition zone.

The time and temperature dependent transformation of opal-A to opal-CT was

modelled for Sites 794 and 795 using fundamental kinetic principles. According to this model, the ratio of opal-A that is converted to opal-CT increased significantly within the opal-CT sediment interval below the transition zone, in comparison with the low precipitation of this mineral phase in the opal-A sediments above the transition. This was due to the higher burial temperature, and therefore higher transformation rates, in the opal-CT zone. One of the main findings based on this kinetic model is that although the peak levels of opal-CT were achieved across the transition zones at 8 and 5 m.y. after initial biogenic silica deposition at Sites 794 and 795, respectively, the transformation of opal-A to opal-CT was not complete until 14 m.y. (Site 794) and 9.5 m.y. (Site 795) after initial sedimentation.

Acknowledgments

This study used data derived from the Deep Sea Drilling Project and Ocean Drilling Program database. We deeply appreciate the editor and reviewers for their constructive comments. Discussions with Raluca Cristina Neagu were much appreciated. The authors declare no conflicts of interest.

References

Agarwal, S. 2019. Engineering chemistry (Fundamntals and applications) (2nd Edition), Cambridge University Press, 1343 p.

Atkins, P., and de Paula, J. 2006. Physical chemistry for the life sciences. Oxford University Press, Oxford, 624 p.

Behl, R.J. 1999. Since Bramlette (1946): The Miocene Monterey Formation of California revisited, *in* Moores, E.M., Sloan, D., and Stout, D.L., eds., Classic Cordilleran Concepts: A View from California: Geological Society of America, Special Papers, v. 338, p. 301–313.

Behl, R.J., and Garrison, R.E. 1994. The origin of chert in the Monterey Formation of California (USA). In Iijima, A., Abed, A., and Garrison, R. (Eds.), Siliceous, phosphatic and glauconitic sediments of the Tertiary and Mesozoic, Proceedings of the 29th International Geological Congress, Part C, Utrecht, The Netherlands, p. 101–132.

Bennett, P.C. 1991. Quartz dissolution in organic-rich aqueous systems, Geochimica et Cosmochimica Acta, v. 55, p. 1781–1797.

Bernhardt, A., Oelze, M., Bouchez, J., von Blanckenburg, F., Mohtadi, M., Christl, M., and Wittmann, H. 2020. $^{10}Be/^{9}Be$ ratios reveal marine authigenic clay formation, Geophysical Research Letters, v. 47, e2019GL086061.

Blum, P. 1997. Physical properties handbook: A guide to the shipboard measurement of physical properties of deep-sea cores: Ocean Drilling Program, Texas A&M University, Technical Note 26.

Bohrmann, G., Kuhn, G., Abelmann, A., Gersonde, R., and Fütterer, D. 1990. A

young porcellanite occurrence from the southwest Indian ridge, Marine Geology, v. 92, p. 155–163.

Botz, R., and Bohrmann, G. 1991. Low-temperature opal-CT precipitation in Antarctic deep- -sea sediments: evidence from oxygen isotopes, Earth and Planetary Science Letters, v. 107, p. 612–617.

Brekke, H. 2000. The tectonic evolution of the Norwegian Sea continental margin with emphasis on the Vøring and Møre basins, in Nøttvedt, A., ed., Dynamics of the Norwegian Margin, Geological Society of London, Special Publication 167, p. 327–378.

Cartwright, J. 2007. The impact of 3D seismic data on the understanding of compaction, fluid flow and diagenesis in sedimentary basins, Journal of the Geological Society of London, v. 164, p. 881–893.

Chaika, C. 1998. Physical properties and silica diagenesis, Stanford University, PhD thesis, 130 p.

Chaika, C., and Dvorkin, J. 1997. Ultrasonic velocities of opaline rocks undergoing silica diagenesis, Geophysical Research Letters, v. 24, p. 2039–2042.

Chaika, C., and Dvorkin, J. 2000. Porosity reduction during diagenesis of

diatomaceous rocks, American Association of Petroleum Geologists Bulletin, v. 84, p. 1173–1184.

Chaika, C., and Williams, L.A. 2001. Density and mineralogy variations as a function of porosity in Miocene Monterey Formation oil and gas reservoirs in California, American Association of Petroleum Geologists Bulletin, v. 85, p. 149–167.

Chang, R. 2005. Physical Chemistry for the Biosciences: Sausalito, California, University Science Books, 772 p.

Clayton, C.J. 1984. The geochemistry of chert formation in Upper Cretaceous chalks. Unpublished PhD Thesis, King's College London.

Compton, J.S. 1991. Porosity reduction and burial history of siliceous rocks from the Monterey and Sisquoc Formation, Point Pedernales area, California, Geological Society of America Bulletin, v. 103, p. 625–636.

Curtis, C.D. 1977. Sedimentary geochemistry: Environments and processes dominated by involvement of an aqueous phase, Philosophical Transactions of the Royal Society, London, v. 286, p. 353–372.

Davies, R.J. 2005. Differential compaction and subsidence in sedimentary basins due to silica diagenesis: A case study, Geological Society of America Bulletin, v. 117, p. 1146–1155.

Davies, R.J. and Cartwright, J. 2002. A fossilized opal A to opal C/T transformation on the northeast Atlantic margin: Support for a significantly elevated palaeo geothermal gradient during the Neogene?, Basin Research, v. 14, p. 467–486.

Davies, R.J., Goulty, N.R., and Meadows, D. 2008. Fluid flow due to the advance of basin-scale silica reaction zones, Geological Society of America Bulletin, v. 120, p. 195–206.

Deep Sea Drilling Project Reports and Publications. 2012. http://deepseadrilling.org

Dove, P.M., and Rimstidt, J.D. 1994. Silica-water interactions, i*n* Prewitt, P.J., et al., eds., Silica-Physical Behavior, Geochemistry and Materials Applications: Washington DC, Mineralogical Society of America, Reviews in Mineralogy, v. 29, p. 259–308.

Dralus, D., Lewan, M.D., and Peters, K. 2015. Kinetics of the opal-A to opal-CT phase transition in low- and high-TOC siliceous shale source rocks: Denver, Colorado, American Association of Petroleum Geologists, Annual Convention &

Exhibition.

Ehlert, C., Doering, K., Wallmann, K., Scholz, F., Sommer, S., Grasse, P., Geilert, S., and Frank, M. 2016. Stable silicon isotope signatures of marine pore waters – Biogenic opal dissolution versus authigenic clay mineral formation, Geochimica et Cosmochimica Acta, v. 191, p. 102-117.

Fisher, A.T., and Becker, K. 1993. A guide to ODP tools for downhole measurements (revised): Ocean Drilling Program, Texas A&M University, Technical Note 10.

Geilert, S., Grasse, P., Doering, K., Wallmann, K., Ehlert, C., Scholz, F., Frank, M., Schmidt, M., and Hensen, C. 2020. Impact of ambient conditions on the Si isotope fractionation in marine pore fluids during early diagenesis, Biogeosciences, v. 17, p. 1745–1763.

Giles, M.R. 1997. Diagenesis: A Quantitative Perspective: Dordrecht, The Netherlands, Kluwer Academic Publishers, 526 p.

Hein, J.R., Scholl, D.W., Barron, J.A., Jones, M.G., and Miller, J. 1978. Diagenesis of late Cenozoic diatomaceous deposits and formation of the bottom simulating reflector in the southern Bering Sea, Sedimentology, v. 25, p. 155–181.

Hesse, R., and Schacht, U. 2011. Early diagenesis of deep-sea sediments, in Hüneke, H., and Mulder, T., et al., eds., Deep-Sea Sediments: Amsterdam, Elsevier, Developments in Sedimentology, v. 63, p. 557–713.

Hinman, N.W. 1990. Chemical factors influencing the rates and sequences of silica phrase transition: Effects of organic constitutions, Geochimica et Cosmochimica Acta, v. 54, p. 1563–1574.

Hinman, N.W. 1998. Sequences of silica phase transitions: Effects of Na, Mg, K, Al, and Fe ions, Marine Geology, v. 147, p. 13–24.

Icenhower, J.P., and, Dove, P.M. 2000. The dissolution kinetics of amorphous silica into sodium chloride solutions: Effects of temperature and ionic strength, Geochimica et Cosmochimica Acta, v. 64, p. 4193–4203.

Iler, R.K. 1973. Colloidal Silica, v. 6, in Surface and Colloid Science, New York, Wiley.

Iler, R.K. 1979. Chemistry of Silica: NewYork, Wiley-Interscience, 866 p.

Ingle, J.C. 1980. Cenozoic paleobathymetry and depositional history of selected sequences within the Southern California Continental Borderland, Cushman Foundation for foraminiferal Research Special Publication, p. 163–195.

Ingle, J.C. 1981. Origin of Neogene diatomites around the north Pacific rim, *in* Garrison, R.E., and Douglas, R.G., eds., The Monterey Formation and Related Siliceous Rocks of California, Society of Economic Paleontologists and Mineralogists Publication, Pacific Section, p. 159–180.

International Ocean Discovery Program. 2014. http://web.iodp.tamu.edu/OVERVIEW/

Ireland, M.T., Goulty, N.R., and Davies, R.J. 2010. Influence of pore water chemistry on silica diagenesis: evidence from the interaction of diagenetic reaction zones with polygonal fault systems, Journal of the Geological Society of London, v. 167, p. 273–279.

Isaacs, C.M. 1981. Porosity reduction during diagenesis of the Monterey Formation, Santa Barbara coastal area, California, *in* Garrison, R.E., Douglas, R.G., Pisciotto, K.E., Isaacs, C.M., and Ingle, J.C., eds., The Monterey Formation and Related Siliceous Rocks of California: San Francisco, California, Society for Sedimentary Geology, Research Symposium, p. 257–271.

Jurkowska, A., Świerczewska-Gładysz, E., Bąk, M., and Kowalik, S. 2019. The role of biogenic silica in the formation of Upper Cretaceous pelagic carbonates and its palaeoecological implications, Cretaceous Research, v. 93, p. 170–187.

Jurkowska, A., and Świerczewska-Gładysz, E. 2020a. New model of Si balance in the Late Cretaceous epicontinental European Basin, Global and Planetary Change, v. 186, p. 103108.

Jurkowska, A., and Świerczewska-Gładysz, E. 2020b. Evolution of Late Cretaceous Si cycling reflected in the formation of siliceous nodules (flints and cherts), Global and Planetary Change, v. 195, p. 103334.

Kastner, M, and Gieskes, J.M. 1983. Opal-A to opal-CT transformation: A kinetic study, i*n* Iijima, A., Hein, J.R., and Siever, R., eds., Siliceous Deposits in the Pacific Region: Amsterdam, Elsevier Science Publishing Company, p. 211–227.

Kastner, M., Keene, J.B., and Gieskes, J.M. 1977. Diagenesis of siliceous oozes – I. Chemical controls on the rate of opal-A to opal-CT transformation – An experimental study, Geochimica et Cosmochimica Acta, v. 41, p. 1041–1059.

Kinoshita, H., and Yamano, M. 1986. The heat flow anomaly in the Nankai Trough area. In Kagami, H., Karig, D.E., Coulbourn, W.T., et al., Initial Reports DSDP, 87: Washington (U.S. Govt. Printing Office), p. 737– 743.

Kinoshita, M., Tobin, H., Ashi, J., Kimura, G., Lallemant, S., Screaton, E.J., Curewitz, D., Masago, H., Moe, K.T. and the Expedition 314/315/316 Scientists. 2009. Proc. IODP, 314/315/316: Washington, DC (Integrated Ocean Drilling

Program Management International, Inc.).

Kuramoto, S., Tamaki, K., Langseth, M.G., Nobes, D.C., Toluyama, H., Pisciotto, K.A., and Taira, A. 1992. Can opal-A/opal-CT BSR be an indicator of the thermal structure of the Yamato Basin, Japan Sea?, *in* Tamaki, K., Suyehiro, K., Allan, J., McWilliams, M., et al., eds., Proceedings of the Ocean Drilling Program, Scientific Results, College Station, Texas , v. 127/128, p. 1145–1156.

Langseth, M.G., and Tamaki, K. 1992. Geothermal measurements: Thermal evolution of the Japan Sea basins and sediments, *in* Tamaki, K., Suyehiro, K., Allan, J., McWilliams, M., et al., eds., Proceedings of the Ocean Drilling Program, Scientific Results, College Station, Texas, v. 127/128 (Pt. 2), p. 1297–1309.

Lancelot, Y. 1973. Chert and silica diagenesis in sediments from the Central Pacific, *in* Winterer, E.L., Ewing, J.I., et al., eds., Initial Reports of the Deep Sea Drilling Project, U.S. Government Printing Office, v. XVII, p. 377–405.

Leeder, M.R. 1982. Sedimentology: Process and Product, London, Allen and Unwin, 344 p.

Littke, R., Fourtanier, E., Thurow, J., and Taylor, E. 1991. Silica diagenesis and its effects on lithification of Broken Ridge deposits, Central Indian Ocean, *in* Peirce, J., Weissel, J., et al., eds., Proceedings of the Ocean Drilling Program, Scientific

Results, College Station, Texas, v. 121, p. 261–272.

Madsen, H.B., Stemmerik, L, and Surlyk, F. 2010. Diagenesis of silica-rich mound-bedded chalk, the Coniacian Arnager Limestone, Denmark, Sedimentary Geology, v. 223, p. 51–60.

Mazzullo, J.M., and Graham, A.G. 1988. Handbook for shipboard sedimentologists: Ocean Drilling Program, Texas A&M University, Technical Note 8.

Meadows, D., and Davies, R.J. 2007. Morphological development of basin-scale silica diagenetic fronts revealed with 2D seismic reflection data: offshore Sakhalin, Russian Far East, Journal of the Geological Society of London, v. 164, p. 1193–1206.

Meadows, D., and Davies, R.J. 2010. The limited suitability of silica diagenetic boundaries as isothermal markers: Insights from seismic reflection imaging, Offshore Sakhalin, Russian Far East, Marine and Petroleum Geology, v. 27, p. 1028–1039.

Michalopoulos, P., and Aller, R.C. 2004. Early diagenesis of biogenic silica in the Amazon delta: Alteration, authigenic clay formation, and storage, Geochimica et Cosmochimica Acta, v. 68, p. 1061-1085.

Migaszewski, Z., Gałuszka, A., Durakiewicz, T., and Starnawska, E. 2006. Middle Oxfordian-Lower Kimmeridgian chert nodules in the Holy Cross Mountains, south-central Poland, Sedimentary Geology, v. 187, p. 11–28.

Mizutani, S. 1970. Silica minerals in the early stage of diagenesis, Sedimentology, v. 15, p. 419–436.

Mizutani, S. 1971. Silica minerals in diagenesis, Memoir 6, The Geological Society of Japan, p. 151–163 (in Japanese).

Mizutani, S. 1977. Progressive ordering of cristobalitic silica in the early stage of diagenesis, Contributions to Mineralogy and Petrology, v. 61, p. 129–140.

Moore, J.C , and Karig, D.E. 1976. Sedimentology, structural geology, and tectonics of the Shikoku subduction zone, southwest Japan, Geological Society of America Bulletin, v. 87, p. 1259–1268.

Mortlock R.A. and Froelich P.N. 1989. A simple method for the rapid deterrnination of biogenic opal in pelagic marine sediment, Deep-Sea Research, v. 36, p. 1415–1426.

Murata, K.J., and Nakata, J.K. 1974. Cristobalitic stage in the diagenesis of diatomaceous shale, Science, v. 184, p. 567–568.

Murray, R.W., Brumsack, H.J., Von Breymann, M.T., Sturz, A.A., Dunbar, R.B., and Gieskes, J.M. 1992a. Diagenetic reactions in deeply buried sediments of the Japan Sea: A synthesis of interstitial water chemistry results from Leg 127 and Leg 128, in Tamaki, K., Suyehiro, K., Allan, L, McWilliams, M., et al., eds., Proceedings of the Ocean Drilling Program: College Station, Texas, Scientific Results, v. 127–128, Pt. 2, p. 1261–1274.

Murray, R.W., Buchholtz, Ten Brink, M.R., Brumsack, H.J., Gerlach, D.C., and Russ, G.P., III. 1992b. Rare earth, major, and trace element composition of Leg 127 sediments, in Pisciotto, K.A., Ingle, J.C., Jr., von Breymann, M.T., Barron, J., et al., eds., Proceeding of the Ocean Drilling Program: College Station, Texas, Scientific Results, v. 127–128, Pt. 1, p. 677–695.

Neagu, R.C. 2011. The relationship between biogenic silica diagenesis and the physical properties of sediments studied using seismic and well data: Cardiff University, PhD thesis, 275 p.

Neagu, R.C., Cartwright, J., Davies, R.J., and Jensen, L. 2010. Fossilisation of a silica diagenesis reaction front on the mid-Norwegian margin, Marine and Petroleum Geology, v. 27, p. 2141–2155.

Nobes, D.C., Murray, R.W., Kuramoto, S., Pisciotto, K.A., and Holler, P. 1992. Impact of silica diagenesis on physical property variations, *in* Pisciotto, K.A., Ingle,

J.C., Jr., von Breymann, M.T., Barron, J., et al., eds., Proceedings of the Ocean Drilling Program, Scientific Results, College Station, Texas, v. 127/128 (Pt. 1).

Ocean Drilling Program Publication Services. 2012. Retrieved from http://www-odp.tamu.edu/publications/

Okada, H., and Bukry, D. 1980. Supplementary modification and introduction of code numbers to the low-latitude coccolith biostratigraphic zonation, Marine Micropaleontology, v. 5, p. 321–325.

Olivarez Lyle, A., and Lyle, M.W. 2002. Determination of biogenic opal in pelagic marine sediments: A simple method revisited. In Lyle, M., Wilson, P.A., Janecek, T.R., et al. (Eds.), Proceedings of the Ocean Drilling Program, Initial Reports, College Station, Texas, v. 199, p. 1–21.

Pickering, R.A., Cassarino, L., Hendry, K.R., Wang, X.L., Maiti, K., and Krause, J.W. 2020. Using stable isotopes to disentangle marine sedimentary signals in reactive silicon pools, Geophysical Research Letters, v. 47, p. e2020GL087877.

Pisciotto, K.A. 1981a. Diagenetic trends in the siliceous facies of the Monterey Shale in the Santa Maria region, California, Sedimentology, v. 28, p. 547–571.

Pisciotto, K.A. 1981b. Distribution, thermal histories, isotopic compositions, and

reflection characteristics of siliceous rocks recovered by the Deep Sea Drilling Project, *in* Warme, J.E., Douglas, R.G., and Winterer, E.L., eds., The Deep Sea Drilling Project: A Decade of Progress, Society of Economic Paleontologists and Mineralogists, Special Publication, No. 32, p. 129–148.

Pisciotto, K.A., Murray, R.W., and Brumsack, H.J. 1992. Thermal history of Japan Sea sediments from isotopic studies of diagenetic silica and associated pore waters, *in* Pisciotto, K.A., Ingle, J.C., Jr., von Breymann, M.T., Barron, J., et al., eds., Proceedings of the Ocean Drilling Program, Scientific Results, College Station, Texas, v. 127/128 (Pt. 1), p. 49–56.

Racki, G., and Cordey, F. 2000. Radiolarian palaeoecology and radiolarites: Is the present the key to the past?, Earth-Science Reviews, v. 52, p. 83–120.

Rahman, S., Aller, R.C., and Cochran, J.K. 2016. Cosmogenic ^{32}Si as a tracer of biogenic silica burial and diagenesis: Major deltaic sinks in the silica cycle, Geophysical Research Letters, v. 43, p. 7124–7132.

Rahman, S., Aller, R.C., and Cochran, J.K. 2017. The missing silica sink: Revisiting the marine sedimentary Si cycle using cosmogenic ^{32}Si, Global Biogeochemical Cycles, v. 31, p. 1559–1578.

Rice, S.B., Freund, H., Huang, W.L., Clouse, J.A., and Isaacs, C.M. 1995.

Application of Fourier Transform Infrared Spectroscopy to silica diagenesis: the opal-A to opal-CT transformation, Journal of Sedimentary Research, v. 65, p. 639–647.

Roaldset, E., and He, W. 1995. Silica-phase transformation of opal-A to opal-CT to quartz: an experimental approach, Trondheim, Norwegian Institute of Technology, Report.

Shipboard Scientific Party. 1981. Site 471: Offshore Magdalena Bay. In Yeats, R. S., Haq, B. U., et al. (Eds.), Initial Reports of the Deep Sea Drilling Project, U.S. Government Printing Office, Washington, v. 63, p. 269–349.

Shipboard Scientific Party. 1990a. Site 794, *in* Tamaki, K., Pisciotto, K., Allan, J., et al., eds., Proceedings of the Ocean Drilling Program, Initial Reports, College Station, Texas, v. 127, p. 71–167.

Shipboard Scientific Party. 1990b. Site 795, *in* Tamaki, K., Pisciotto, K., Allan, J., et al., eds., Proceedings of the Ocean Drilling Program, Initial Reports, College Station, Texas, v. 127, p. 169–245.

Shipboard Scientific Party. 1990c. Site 799. In Ingle, J. C., Jr., Suyehiro, K., von Breymann, M. T., et al. (Eds.), Proceedings of the Ocean Drilling Program, Initial Reports, College Station, Texas, v. 128, p. 237–402.

Shipboard Scientific Party. 1997a. Site 1016, *in* Lyle, M., Koizumi, I., Richter, C., et al., eds., Proceedings of the Ocean Drilling Program, Initial Reports, College Station, Texas, v. 167, p. 239–283.

Shipboard Scientific Party. 1997b. Site 1022, *in* Lyle, M., Koizumi, I., Richter, C., et al., eds., Proceedings of the Ocean Drilling Program, Initial Reports, College Station, Texas, v. 167, p. 461–495.

Shipboard Scientific Party. 2001a. Site 1172. In Exon, N. F., Kennett, J. P., Malone, M. J., et al. (Eds.), Proceedings of the Ocean Drilling Program, Initial Reports, College Station, Texas, v. 189, p. 1–149.

Shipboard Scientific Party. 2001b. Site 1173. In Moore, G. F., Taira, A., Klaus, A., et al. (Eds.), Proceedings of the Ocean Drilling Program, Initial Reports, College Station, Texas, v. 190, p. 1–147.

Shipboard Scientific Party. 2002. Site 1207, *in* Bralower, T.J., Premoli Silva, I., Malone, M.J., et al., eds., Proceedings of the Ocean Drilling Program, Initial Reports, College Station, Texas, v. 198, p. 1–140.

Singh, B., and Gilkes, R.J. 1993. The recognition of amorphous silica in indurated soil profiles, Clay Minerals, v. 28, p. 461–474.

1517 Tada, R. 1991. Compaction and cementation in siliceous rocks and their possible
1518 effect on bedding enhancement, *in* Einsele, G., Ricken, W., and Seilacher, A., eds.,
1519 Cycles and Events in Stratigraphy: Berlin, Springer-Verlag, p. 480–491.
1520
1521 Tatzel, M., von Blanckenburg, F., Oelze, M., Schuessler, J.A., and Bohrmann, G.
1522 2015. The silicon isotope record of early silica diagenesis, Earth and Planetary
1523 Science Letters, v. 428, p. 293–303.
1524
1525 The Shipboard Scientific Party. 1973. Site 184, in Scholl, D.W., Creager, J.S.,
1526 Boyce, R.E., et al., (Eds.), Initial Reports of the Deep Sea Drilling Project, U.S.
1527 Government Printing Office, Washington, v. 63, p. 93–167.
1528
1529 Van Cappellen, P., and Qiu, L. 1997a. Biogenic silica dissolution in sediments of the
1530 Southern Ocean. I. Solubility: Deep-Sea Research, Part II: Topical Studies in
1531 Oceanography, v. 44, p. 1109–1128.
1532
1533 Van Cappellen, P., and Qiu, L. 1997b. Biogenic silica dissolution in sediments of the
1534 Southern Ocean. II. Kinetics: Deep-Sea Research, Part II: Topical Studies in
1535 Oceanography, v. 44, p. 1129–1149.
1536
1537 Varkouhi, S. 2018. Biogenic silica diagenesis under early burial in hemipelagic
1538 marine sediments, University of Oxford, DPhil thesis, 428 p.
1539

Varkouhi, S., and Wells, J. 2020. The relation between temperature and silica benthic exchange rates and implications for near-seabed formation of diagenetic opal, Results in Geophysical Sciences, v. 1–4, p. 100002.

Varkouhi, S., Cartwright, J.A., and Tosca, N.J. 2020a. Anomalous compaction due to silica diagenesis — Textural and mineralogical evidence from hemipelagic deep-sea sediments of the Japan Sea, Marine Geology, v. 426, p. 106204.

Varkouhi, S., Tosca, N.J., and Cartwright, J.A. 2020b. Pore water chemistry – A proxy for tracking the signature of ongoing silica diagenesis, Journal of Sedimentary Research, v. 90, p. 1–31.

Weller, R., and Behl, R.J. 2015. Physical and Mechanical Characteristics of the opal-A to opal-CT transition zone: Enhanced diatomite permeability from heterogeneous diagenetic embrittlement: Oxnard, California, Pacific Section of American Association of Petroleum Geologists, Society of Economic Geologists, and Society for Sedimentary Geology, Joint Technical Conference.

Williams, L.A., and Crerar, D.A. 1985. Silica diagenesis, II. General mechanisms, Journal of Sedimentary Petrology, v. 55, p. 312–321.

Williams, L.A., Parks, G.A., and Crerar, D.A. 1985. Silica diagenesis, I. Solubility controls, Journal of Sedimentary Petrology, v. 55, p. 301–311.

Wise, S.W., Buie, B.F., and Weaver, F.M. 1972. Chemically precipitated sedimentary cristobalite and the origin of chert, Eclogae Geologicae Helvetiae, v. 65 , p. 157–163.

Worden, R.H., and Burley, S.D. 2003. Sandstone diagenesis: the evolution of sand to stone, *in* Burley, S.D., and Worden, R.H. (eds.,), Sandstone Diagenesis: Recent and Ancient. Blackwell Publishing, p. 1–44.

Wrona, T., Jackson, C.A.-L., Huuse, M., and Taylor, K.G. 2017. Silica diagenesis in Cenozoic mudstones of the North Viking Graben: physical properties and basin modelling, Basin Research, v. 29, p. 556–575.

Zijlstra, H.J.P. 1987. Early diagenetic silica precipitation, in relation to redox boundaries and bacterial metabolism, in late Cretaceous chalk of the Maastrichtian type locality, Geologie en Mijnbouw, v. 66, p. 345–355.

Zijlstra, J.J.P. 1994. Sedimentology of the Late Cretaceous and Early Tertiary (tuffaceous) chalk of northwest Europe, Faculteit Aardwetenschappen (cit. on p. 25).

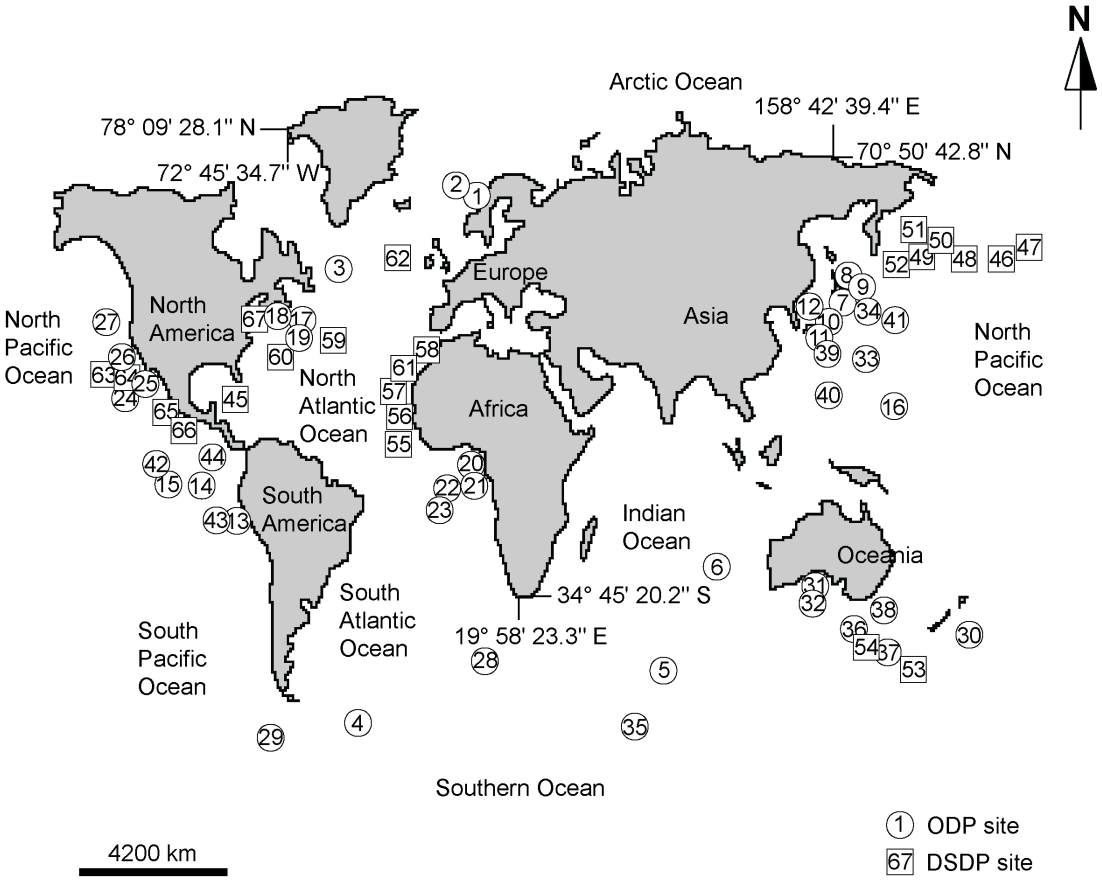

1587 Figure 1. Location of the investigated borehole sites.

1588 ODP sites (circled numbers): 1) 642/Leg 104, 2) 643/Leg 104, 3) 647/Leg 105, 4)
1589 696/Leg 113, 5) 748/Leg 120, 6) 752/Leg 121, 7) 794/Leg 127, 8) 795/Leg 127, 9)
1590 796/Leg 127, 10) 797/Leg 127, 11) 798/Leg 128, 12) 799/Leg 128, 13) 846/Leg 138,
1591 14) 847/Leg 138, 15) 850/Leg 138, 16) 869/Leg 143, 17) 902/Leg 150, 18) 903/Leg
1592 150, 19) 904/Leg 150, 20) 959/Leg 159, 21) 960/Leg 159, 22) 961/Leg 159, 23)
1593 962/Leg 159, 24) 1010/Leg 167, 25) 1011/Leg 167, 26) 1016/Leg 167, 27) 1022/Leg
1594 167, 28) 1090/Leg 177, 29) 1095/Leg 178, 30) 1122/Leg 181, 31) 1132/Leg 182, 32)
1595 1133/Leg 182, 33) 1149/Leg 185, 34) 1150/Leg 186, 35) 1165/Leg 188, 36)
1596 1170/Leg 189, 37) 1171/Leg 189, 38) 1172/Leg 189, 39) 1173/Leg 190, 40)
1597 1201/Leg 195, 41) 1207/Leg 198, 42) 1225/Leg 201, 43) 1226/Leg 201, 44)
1598 1256/Leg 206;
1599 DSDP sites (numbers inside squares): 45) 98/Leg 11, 46) 184/Leg 19, 47) 185/Leg
1600 19, 48) 188/Leg 19, 49) 189/Leg 19, 50) 190/Leg 19, 51) 191/Leg 19, 52) 192/Leg
1601 19, 53) 277/Leg 29, 54) 280/Leg 29, 55) 366/Leg 41, 56) 367/Leg 41, 57) 368/Leg
1602 41, 58) 370/Leg 41, 59) 385/Leg 43, 60) 387/Leg 43, 61) 397/Leg 47, 62) 405/Leg
1603 48, 63) 467/Leg 63, 64) 469/Leg 63, 65) 471/Leg 63, 66) 473/Leg 63, 67) 603/Leg
1604 93
1605
1606

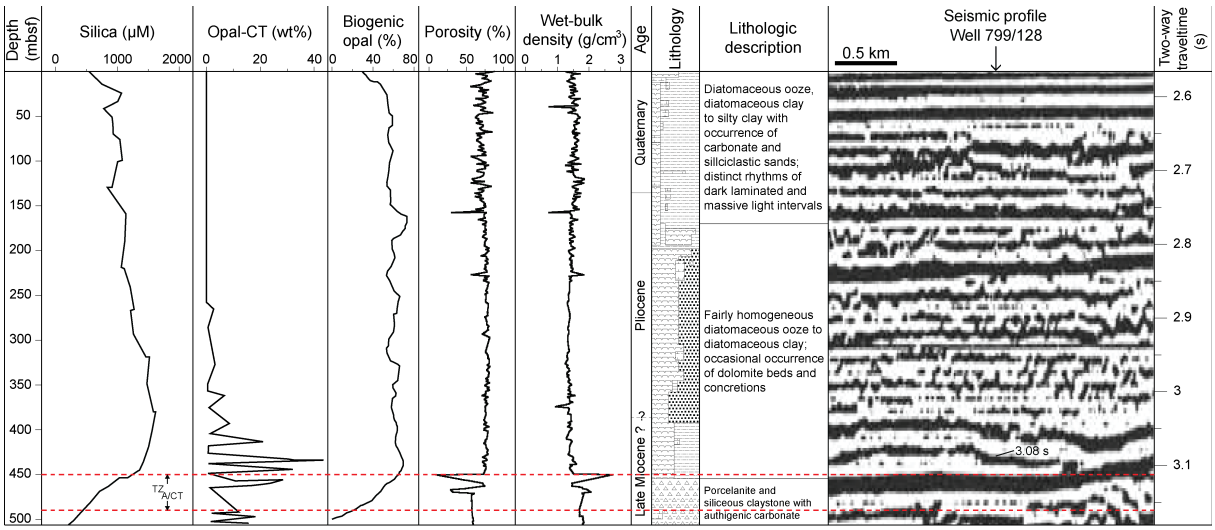

1608 Figure 2. Example of a representative ODP borehole, Well 799/Leg 128 illustrating
1609 the correlation of abrupt petrophysical (density and porosity) variations with opal-A
1610 content of sediment, silica sink, and appearance of porcellanites across the depth of
1611 an opal-A to opal-CT transition penetrated at this site. Note these sharp contrasts are
1612 not coincident with the distribution of XRD-determined diagenetic opal at this
1613 boundary, but are almost tied to a high amplitude reflection on the seismic section at
1614 3.08 s. 0.1 s two-way travel-time roughly equates to 84 m sediment thickness in this
1615 profile (the data in this figure were derived and modified from Shipboard Scientific
1616 Party, 1990c).

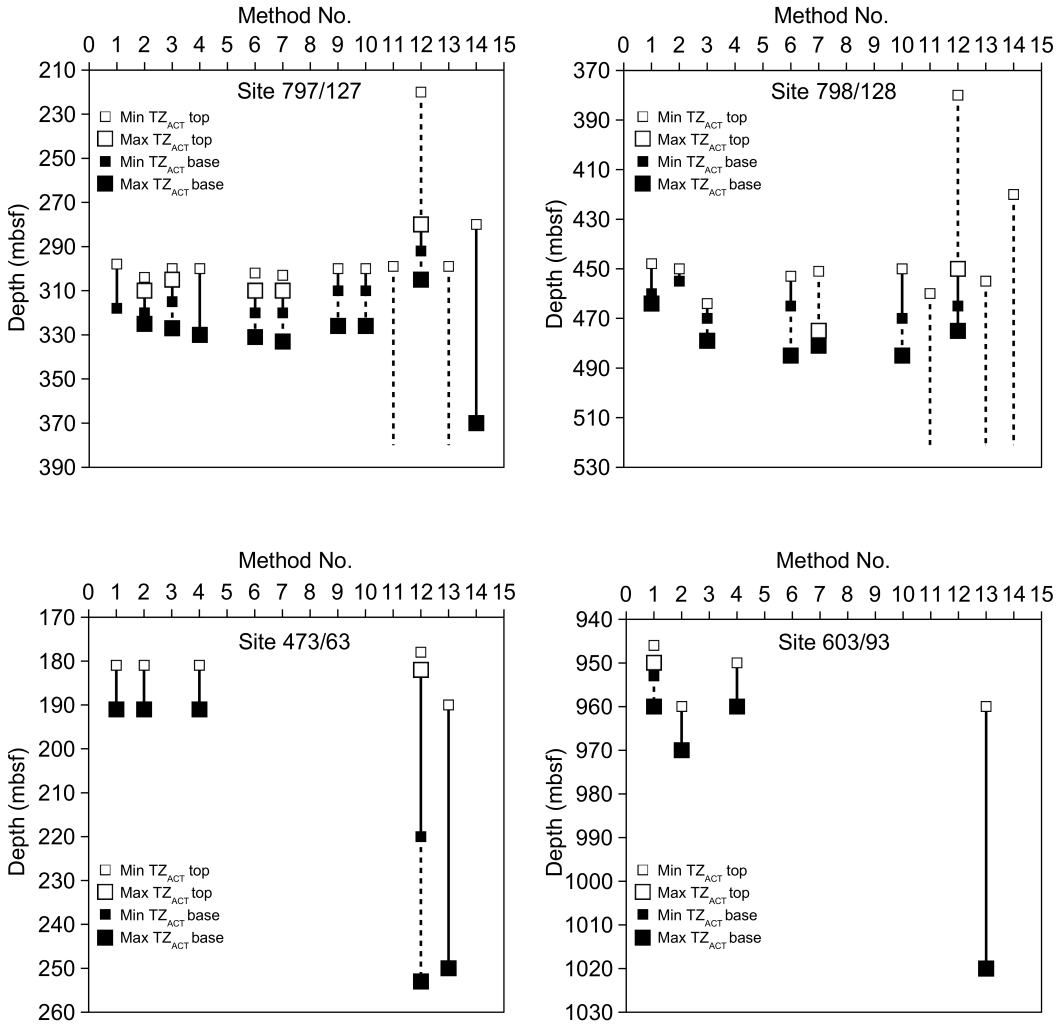

1618 Figure 3. $TZ_{A/CT}$ thickness as estimated by changes in the physical properties of the
1619 sediments for four representative borehole sites. The depth constraints of this
1620 boundary using XRD, smear slides, lithological features, and pore-water chemistry
1621 are also plotted for comparison. Some of the measurements at Sites 797 and 798
1622 were modified from Neagu (2011). Due to low-resolution sampling spacings, the
1623 minimum and maximum symbols could not be determined for few data types. Given
1624 the poor recovery of the core samples, measurements of physical properties for the
1625 DSDP sites are often absent.

1626 Numbers on the abscissa represent the downhole measurement methods (1 = bulk density, 2
1627 = P-wave velocity, 3 = gamma ray, 4 = porosity, 5 = resistivity) and measurements directly
1628 on core samples (6 = wet-bulk density, 7 = porosity, 8 = P-wave velocity, 9 = gamma ray, 10
1629 = thermal conductivity, 11 = XRD, 12 = smear slides, 13 = descriptive lithology, 14 =
1630 dissolved silica concentration) used for determining the thickness of the $TZ_{A/CT}$.

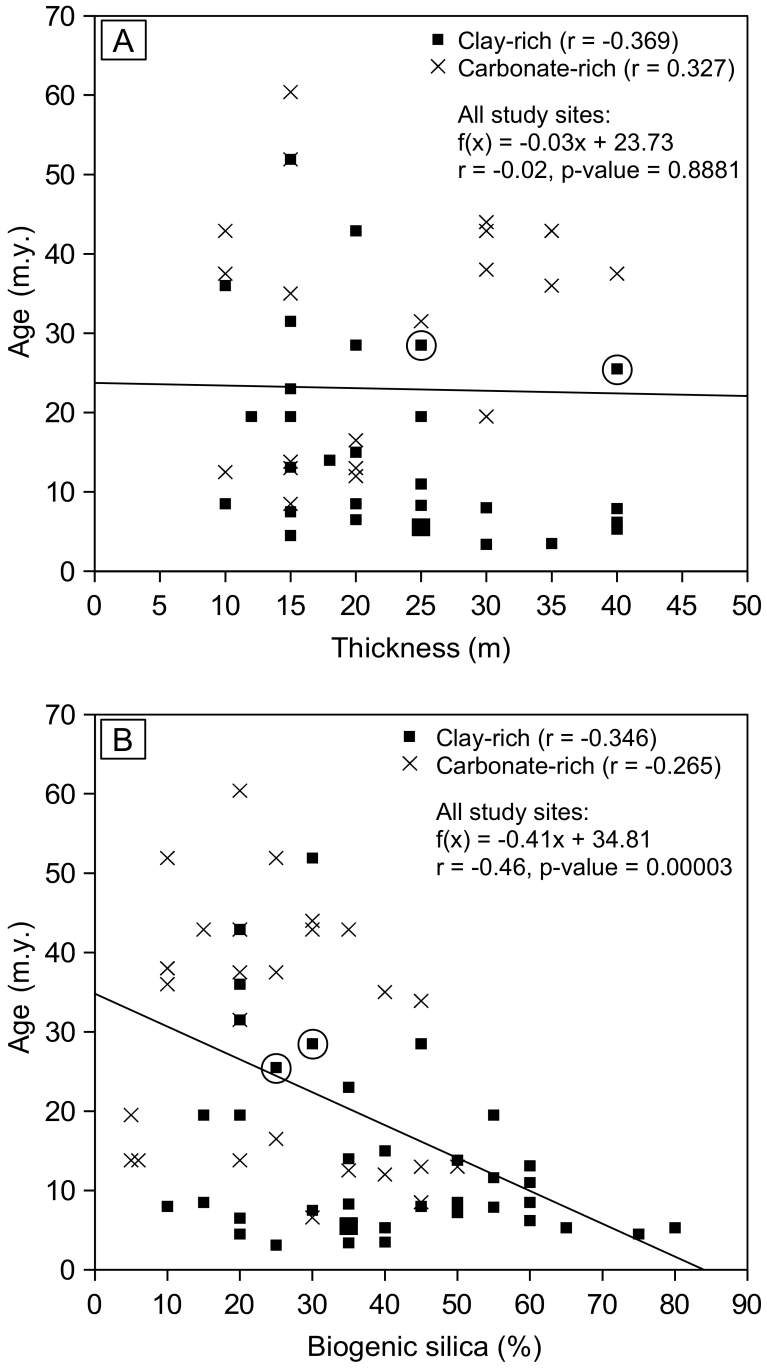

1632 Figure 4. A) Cross-plot illustrating the relationship between the $TZ_{A/CT}$ age and
1633 thickness in clay-dominated (solid squares) and carbonate-dominated (× marks)
1634 sediments; B) Age of the $TZ_{A/CT}$ relative to the opal content of the sediment hosting
1635 the $TZ_{A/CT}$. In both Figures 4A, B, circled squares denote Sites 902/150 and 903/150
1636 where $TZ_{A/CT}$ depth was uncertain.

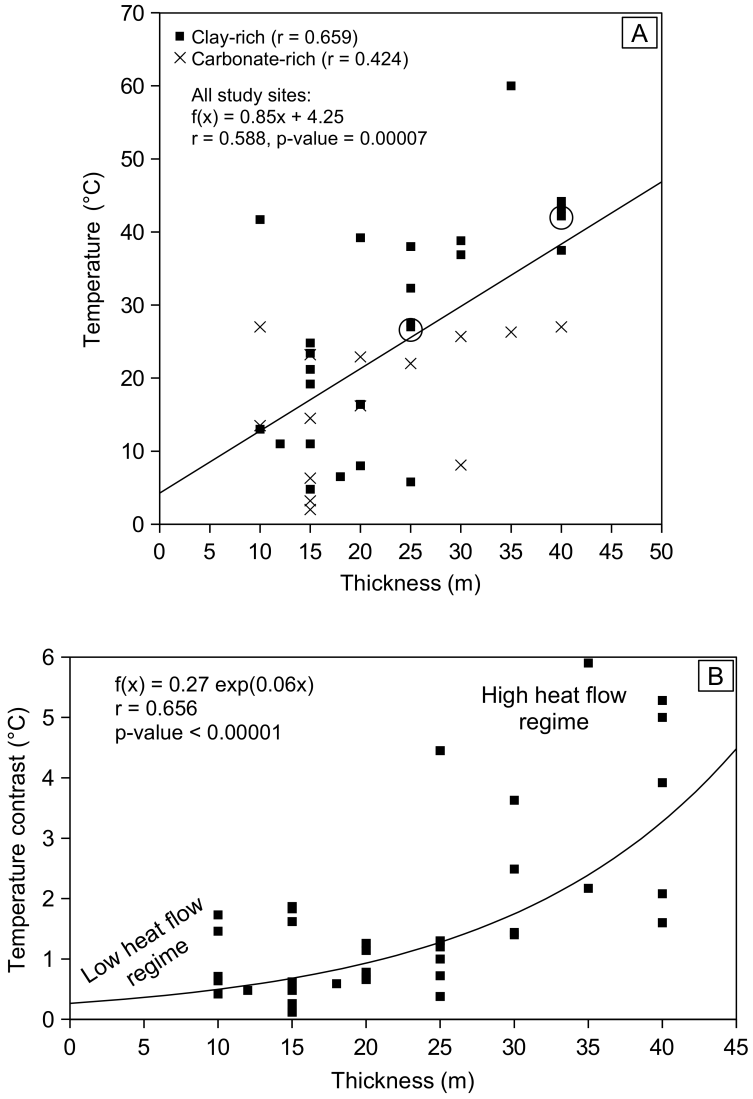

Figure 5. A) Scatterplot showing the $TZ_{A/CT}$ temperature–zone thickness relationship in clay- and carbonate-dominated ODP and DSDP study sites. Values for some of the ODP sites were derived and modified from Neagu (2011). The explanations for the circled data points are given in Figure 4; B) Temperature contrast through the $TZ_{A/CT}$ versus zone thickness for the studied sites. The temperature contrast between top and bottom of the $TZ_{A/CT}$ was calculated using the equation: $\Delta T = G\delta$, where ΔT is the temperature difference (°C) between the top and bottom of the zone, G is the geothermal gradient of the sediment column hosting the $TZ_{A/CT}$ (in °C/m), and δ is the $TZ_{A/CT}$ thickness (in m). Note that the low and high values of temperature difference between the frontiers of the $TZ_{A/CT}$ correspond to low and high heat flow conditions in the host sediment, respectively.

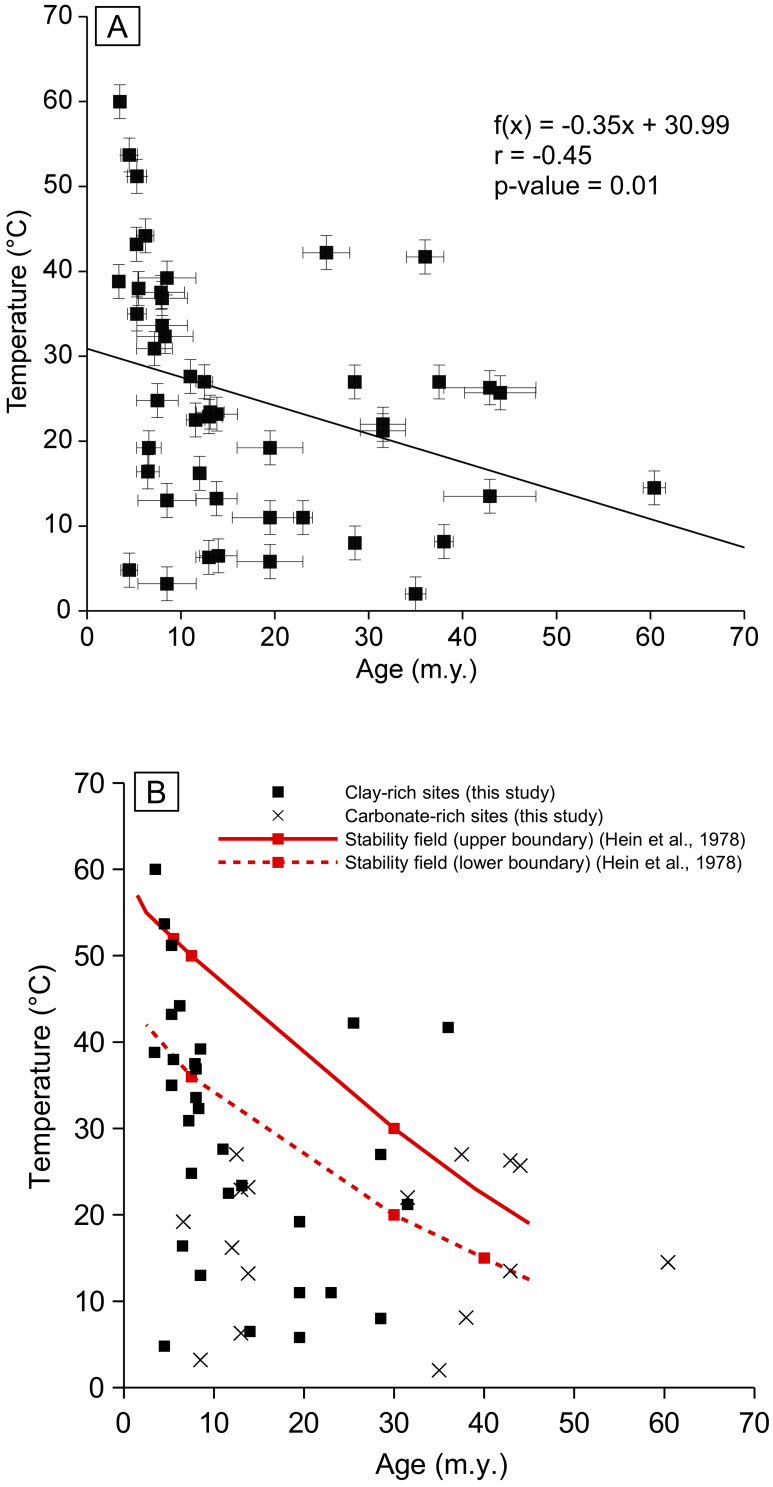

Figure 6. A) Inverse relationship between age and *in situ* temperature across the $TZ_{A/CT}$ at the studied ODP and DSDP sites. Data for some of the ODP sites were modified from Neagu (2011).The p-value (< significance level 0.05) shows this

relationship is statistically significant (Noymer, 2008). The X- and Y-error bars represent the possible age ranges of the sediment and the standard errors, respectively; B) The age–temperature data points of Figure 6A as classified by their dominant host sediment types. There is a moderate inverse correlation between these variables for clay-rich sites, while a weak anticorrelation for carbonate sediments (Noymer, 2008). The data of Hein et al. (1978) are also plotted for comparison. The continuous and dashed red lines represent the upper and lower limits of opal-CT formation as determined by the Hein et al. (1978) data.

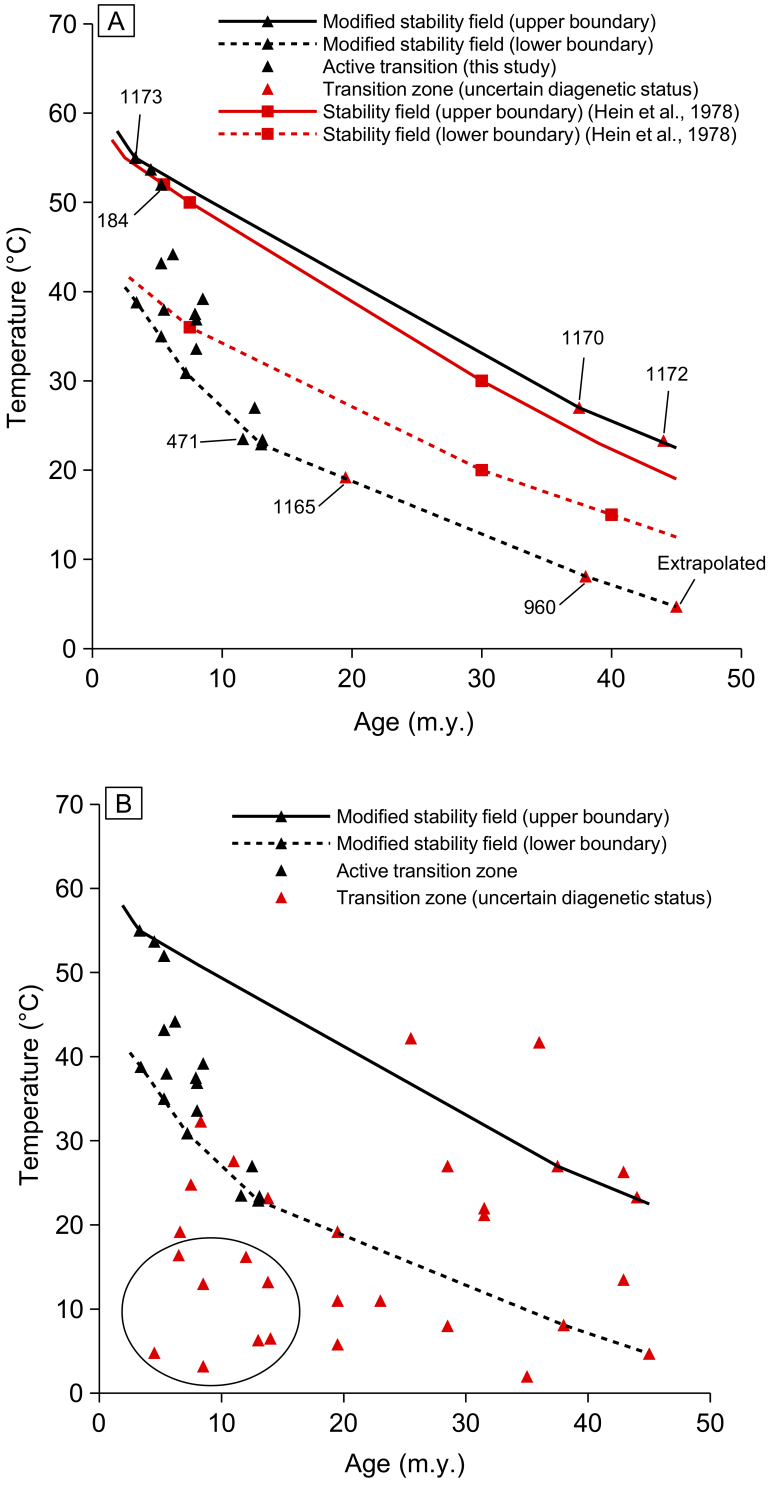

1682 Figure 7. A) Stability field of diagenetic silica (opal-CT) formation based on age and
1683 temperature values at the $TZ_{A/CT}$ depths analysed in this study. The continuous and
1684 dashed black lines represent the upper and lower boundaries of this stability field,

respectively. The age and temperature of the $TZ_{A/CT}$ at Site 1173 as well as the $TZ_{A/CT}$ temperature at Sites 184, 471, and 1172 were slightly modified (these sites are labelled on the diagram). The data of Hein et al. (1978) are shown for comparison. The continuous and dashed red lines represent the original upper and lower limits of the opal-CT stability field as defined by Hein et al. (1978); B) Distribution of the $TZ_{A/CT}$ temperature and time data from the studied ODP and DSDP sites within and around the extended stability field of opal-CT formation. The frontiers of the stability field are based on the data points from active transitions, and extrapolated using the data points representing transitions with uncertain diagenetic status, but fitting the inverse temperature–age correlation for ongoing silica diagenesis (red triangles connected with continuous and dashed black lines). The circled data points represent likely arrested transitions (Sites 473, 846, 850, 1095, 1133, 1149, 1201, 1225; Appendix I).

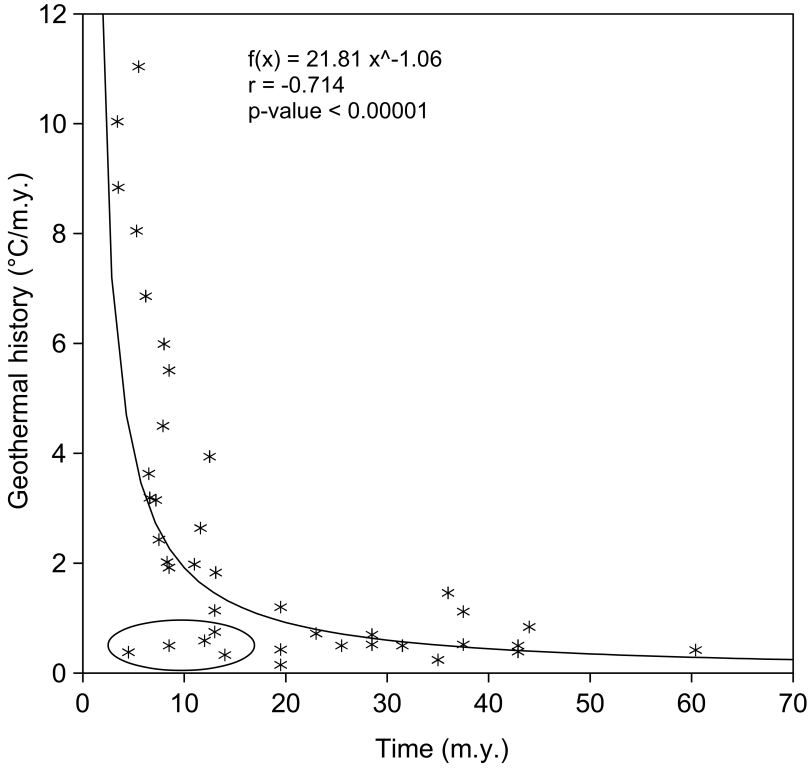

Figure 8. Geothermal evolution versus age at the $TZ_{A/CT}$ for the study sites. Data for some of the ODP wells were modified from Neagu (2011).The temperature history values on the Y-axis are the product of geothermal gradient (in °C/m) and sedimentation rate (in m/m.y.) at each site. Note the negative correlation between the two variables. The correlation is significant at p-value < significance level 0.05 (Noymer, 2008). The circled data points represent likely arrested transitions.

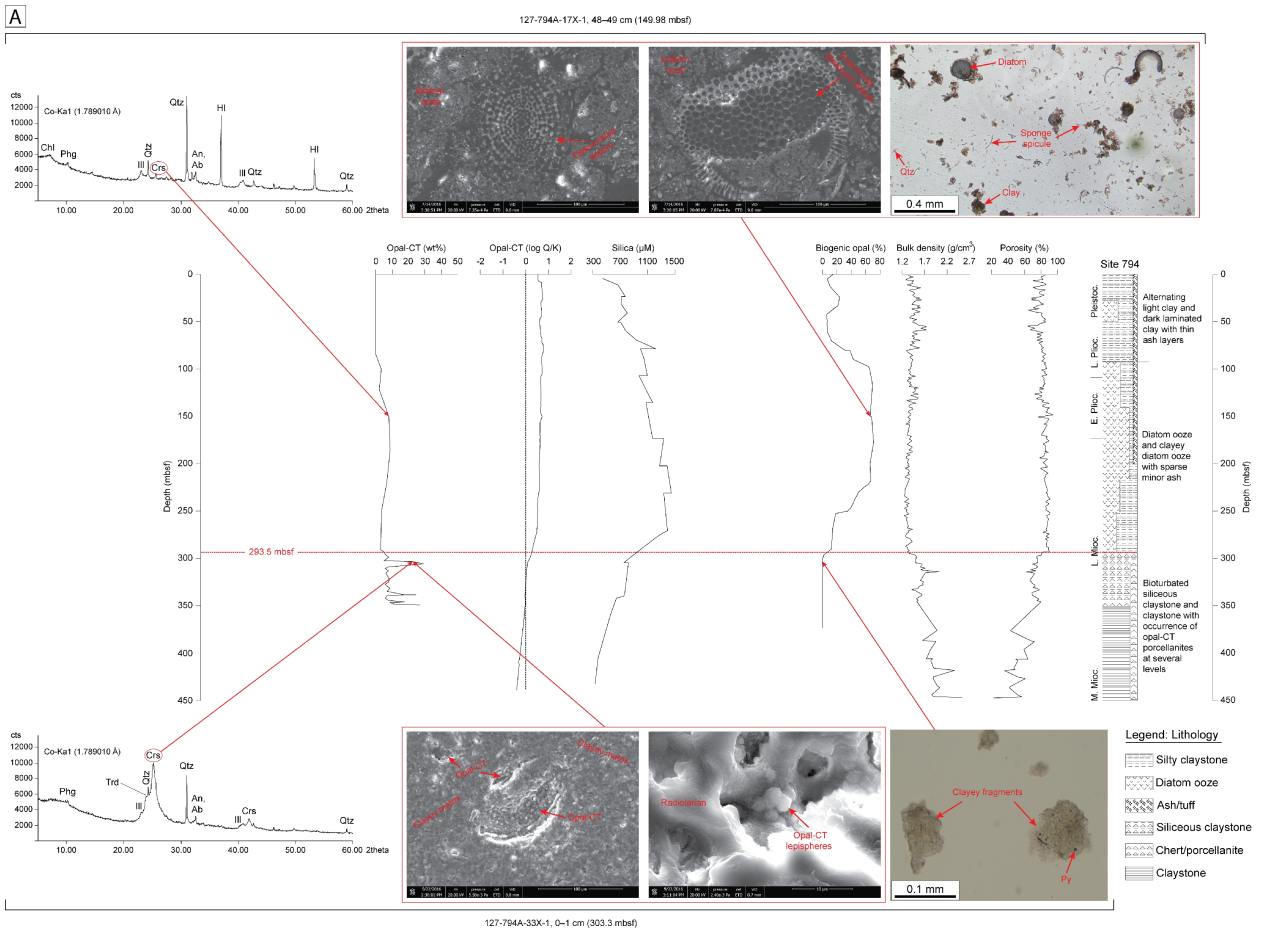

1723 Figure 9. Correlation of porosity and density contrasts with lithological features,
1724 opal-A depression, silica sink, and near-equilibrium pore-water saturation index with
1725 respect to opal-CT across the penetrated opal-A to opal-CT reaction front, Sites 794
1726 (A) and 795 (B). Black dashed lines represent solubility equilibrium (log Q/K = 0).
1727 Red dashed lines denote top of the petrophysical $TZ_{A/CT}$. These sudden contrasts do
1728 not coincide with the distribution of diagenetic opal as determined by XRD. The
1729 lithological, petrophysical, and dissolved silica data in this figure were derived from
1730 Shipboard Scientific Party (1990a, 1990b) and International Ocean Discovery
1731 Program (2014), the diagenetic opal (XRD analyses) and biogenic silica values,
1732 thermodynamic data, and smear-slides and SEM photomicrographs from Varkouhi
1733 (2018), Varkouhi et al. (2020a), and Varkouhi et al. (2020b).

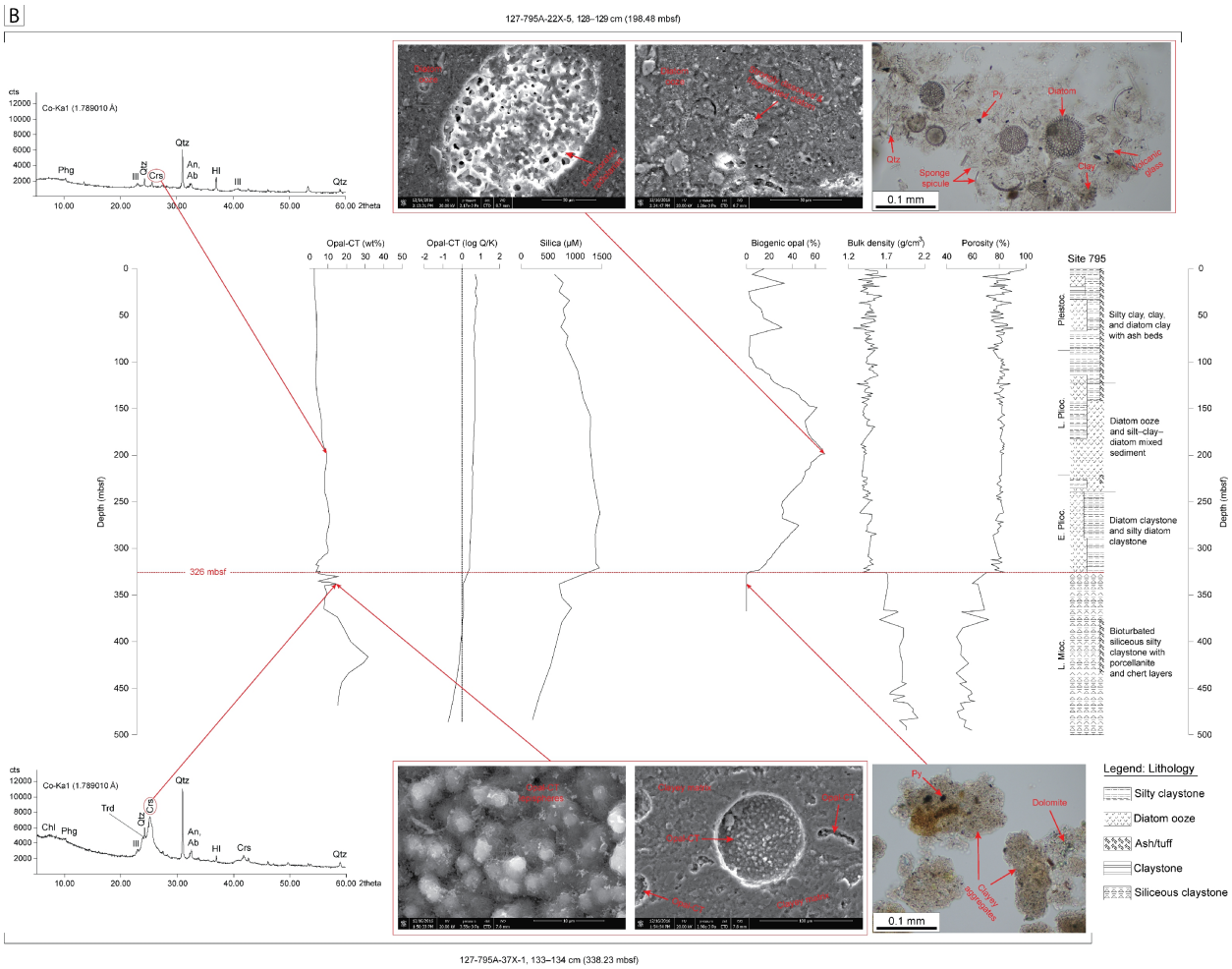

1734 Figure 9. Continued.

1735

1736

1737

1738

1739

1740

1741

1742

1743

1744

1745

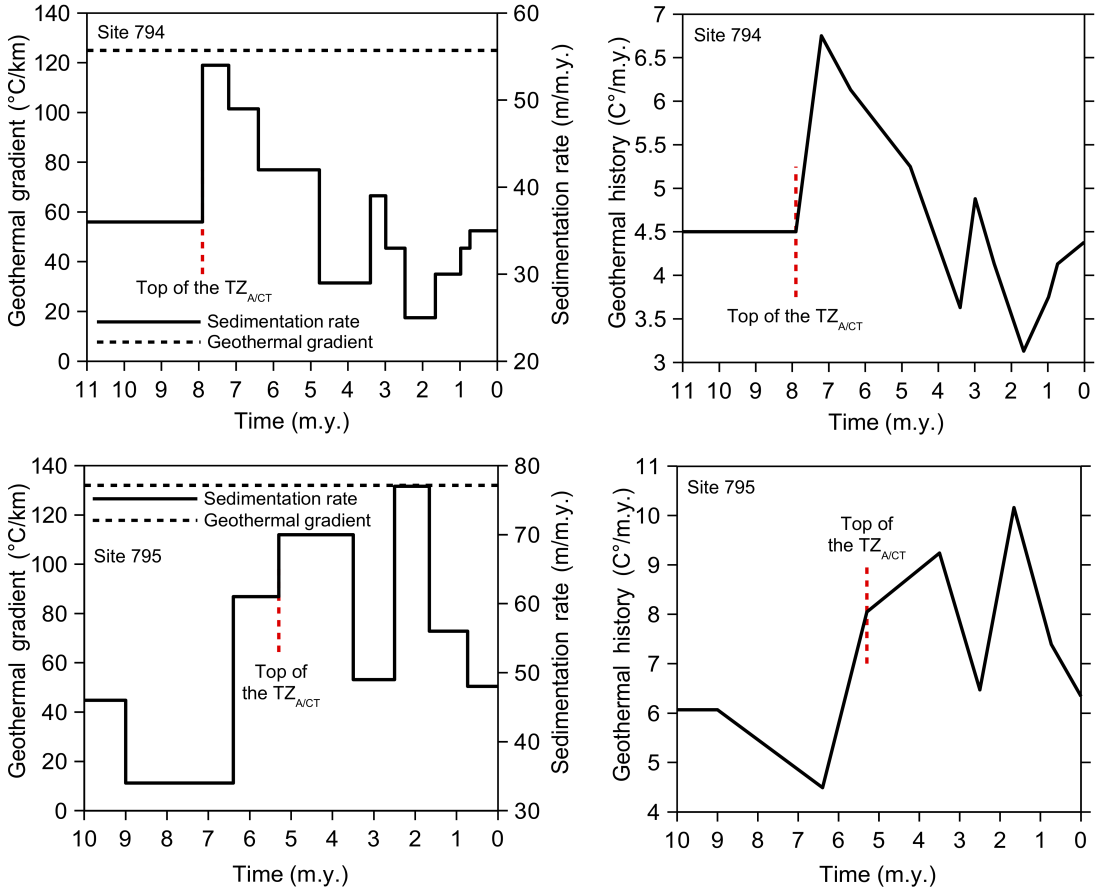

1746 Figure 10. Reconstructed burial and thermal histories for the sediments hosting the
1747 $TZ_{A/CT}$ at Sites 794 and 795. The numerical age of the sediments was derived from
1748 the depth profiles of diatom zones and magnetostratigraphic datum levels provided in
1749 the ODP 794 and 795 initial reports (see Shipboard Scientific Party, 1990a, b).
1750
1751
1752
1753
1754
1755
1756
1757
1758

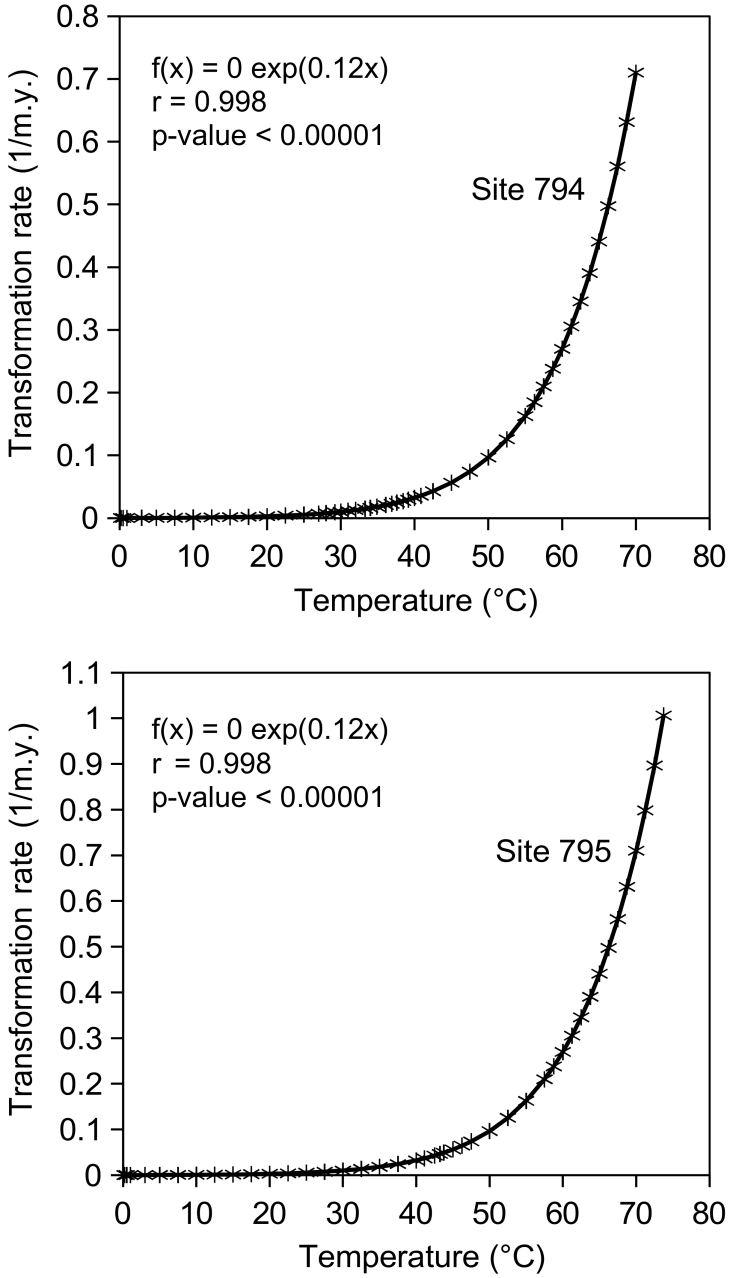

Figure 11. Calculated opal-A to opal-CT transformation rates versus *in situ* temperature measurements at ODP Sites 794 and 795.

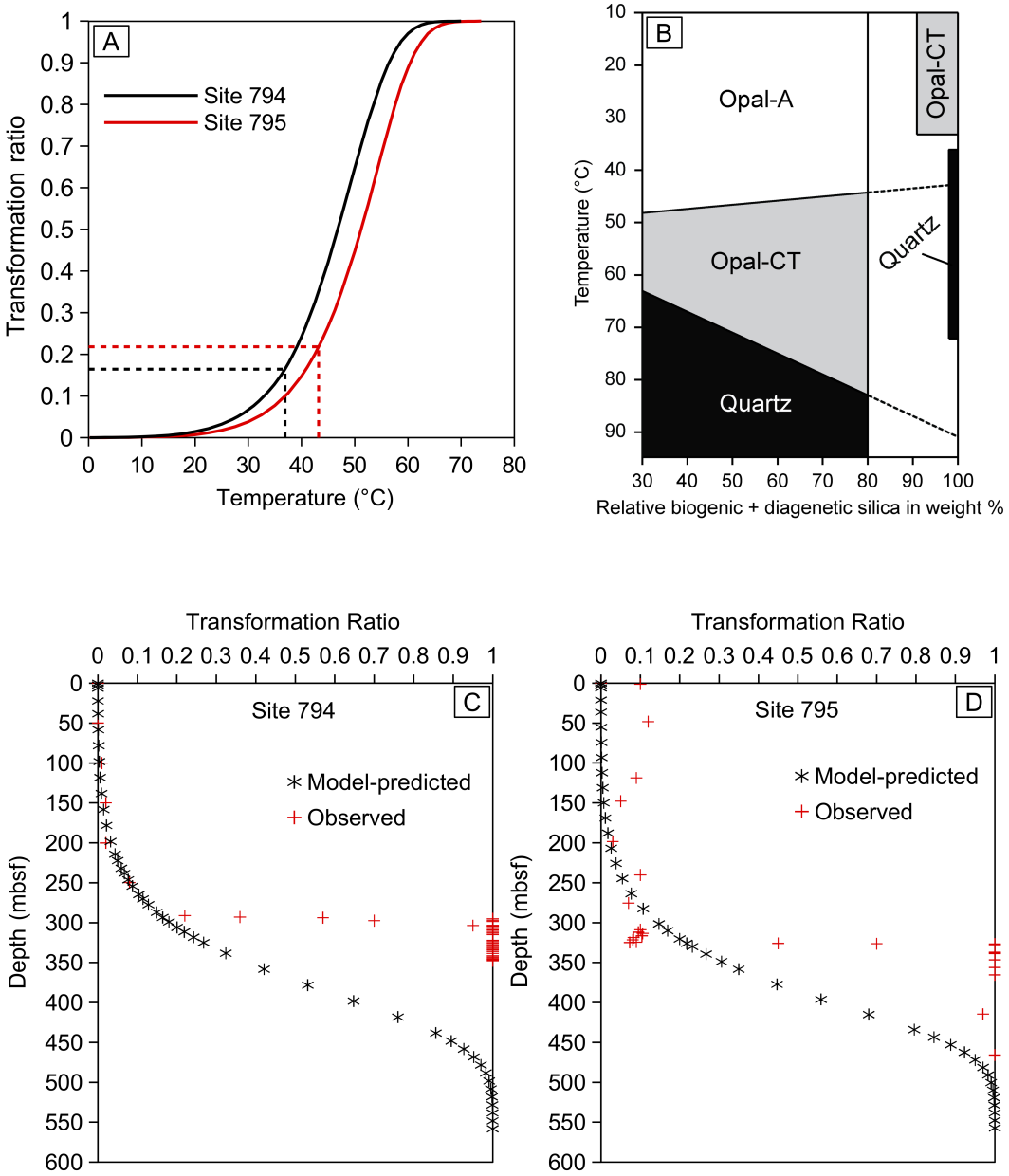

1765 Figure 12. A) Modelled opal-A to opal-CT transformation at ODP Sites 794 and 795. Black
1766 and red dotted lines mark the coordinates of the $TZ_{A/CT}$ at Sites 794 and 795, respectively; B)
1767 Reference phase diagram for silica diagenesis (redrawn from Behl, 1999); C) Comparison
1768 between modelled and observed transformation ratios in Site 794; D) Comparison of
1769 modelled and observed transformation ratios at Site 795. The observed transformation ratios
1770 plotted in Figures 12C, D have been approximated by combining the results of smear-slide
1771 analyses (Varkouhi, 2018; Varkouhi et al., 2020a) and the results of the quantitative X-ray
1772 diffraction of the sediments from these two sites (Varkouhi et al., 2020b) to determine the
1773 amount of biogenic and diagenetic silica in the sediment.

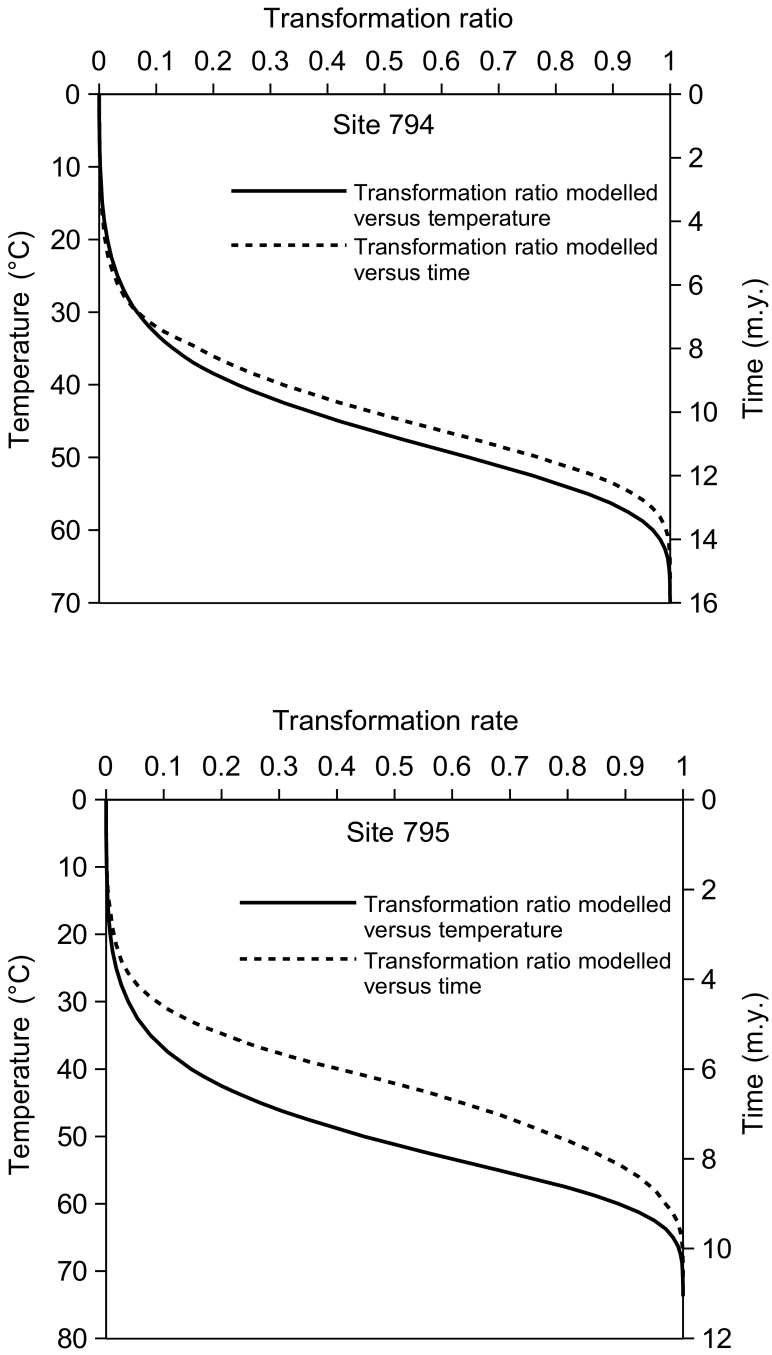

Figure 13. Modelled transformation of opal-A to opal-CT as a function of temperature and time. Sediment numerical ages were derived from the ODP 794 and 795 initial reports (see Shipboard Scientific Party, 1990a, b).

Table 1. Likely active opal-A to opal-CT transition zones involved in this study and their characteristics. The data were extracted from the ODP and DSDP database. No. = the identification number of the sites presented in Figure 1. The symbols represent: ✓ = yes, – = no data

No.	Site	Stratigraphic continuity	Sediment age, m.y.	Biosilica, %	Geothermal gradient, °C/km	*In situ* temperature, °C	Silica concentration drop at the $TZ_{A/CT}$
7	794	✓	7.9	55	125	37.5	✓
8	795	✓	5.3	40	132	43.2	✓
9	796	✓	5.5	35	178	38	✓
10	797	✓	8	45	121	36.9	✓
11	798	✓	3.4	35	83	38.8	✓
12	799	✓	6.2	60	98	44.2	✓
24	1010	✓	13.1	60	122	23.4	–
26	1016	✓	7.2	50	105	30.9	–
27	1022	✓	8	10	88	33.6	–
39	1173	✓	3.5	40	170	60	✓
43	1226	✓	13	45	57.2	22.9	✓
44	1256	✓	12.5	35	146	27	✓
46	184*	✓	5.3	80	82	51.2	–
47	185*	✓	5.3	65	50.4	35	–
48	188*	✓	4.5	75	–	–	–
49	189*	✓	4.5	20	95.8	53.7	–
50	190*	✓	5.3	40	–	–	–
51	191*	✓	3.1	25	–	–	–
52	192*	✓	8.5	60	–	–	–
63	467	✓	8.5	50	63	39.2	–
65	471	✓	11.6	55	132	22.5	–

* The temperature and age data from Sites 184, 185, 188, 189, 190, 191, and 192 (DSDP Leg 19) are a major component of the Hein et al. (1978) reference stability field. The values estimated by Hein et al. (1978) for these sites were slightly modified in this study, using them to define the new stability field for the initiation of opal-CT precipitation.

Appendix I. Parameters of the ODP and DSDP sites comprising the opal-A to opal-CT transition zone. The values were mostly extracted or derived from ODP and DSDP datasets. Values for some of the ODP sites were derived or modified from Neagu (2011), and the age and temperature values for the DSDP Sites 184, 185, 188, 189, 190, 191, and 192 derived and slightly modified from Hein et al. (1978). No. = the identification number of the sites presented in Figure 1, BSi = mean biogenic silica in the total volume of the sediment column hosting and overlying the silica transition, Φ_A = mean porosity of the sediments rich in opal-A, Φ_{CT} = mean porosity of the sediments rich in opal-CT, $\Delta\Phi$ = difference between the mean porosity of opal-CT- and opal-A-rich sediments, ρ_A = mean bulk density of the sediments rich in opal-A, ρ_{CT} = mean bulk density of sediments rich in opal-CT, $\Delta\rho$ = difference between the mean bulk density of opal-CT- and opal-A-rich sediments, V_A = mean velocity in the sediments rich in opal-A, V_{CT} = mean velocity in the sediments rich in opal-CT, ΔV = difference between the mean velocity in opal-CT- and opal-A-rich sediments, R_A = mean resistivity of sediments rich in opal-A, R_{CT} = mean resistivity of sediments rich in opal-CT, ΔR = difference between the mean resistivity of opal-CT- and opal-A-rich sediments, G = present-day geothermal gradient of the sediment column hosting the silica diagenetic transition, Q = present-day heat flow of the sediment column hosting the silica transition zone, ω = mean sedimentation rate for the period immediately following the deposition of biogenic opal

No.	Leg	Site	Water depth, m	Dominant lithology	$TZ_{A/CT}$ depth, mbsf	$TZ_{A/CT}$ age, m.y.	BSi, %	Φ_A, %	Φ_{CT}, %	$\Delta\Phi$, %	ρ_A, g/cm^3	ρ_{CT}, g/cm^3	$\Delta\rho$, g/cm^3	V_A, km/s	V_{CT}, km/s	ΔV, km/s	R_A, Ω.m	R_{CT}, Ω.m	ΔR, Ω.m	$TZ_{A/CT}$ temperature, °C	$TZ_{A/CT}$* thickness, m	G, °C/km	Q, mW/m^2	ω, m/m.y.
1	ODP 104	642	1292	Clay	275	23	35	78	62	16	1.45	1.8	0.35	1.7	1.85	0.15	–	–	–	11	15	40	90.4	18
2	ODP 104	643	2768	Clay	270	19.5	55	70	45	25	1.4	1.65	0.25	1.5	2	0.5	–	–	–	11	12	40	90.4	30
3	ODP 105	647	3869	Clay	240	28.5	45	70	55	15	1.45	1.8	0.35	1.6	1.65	0.05	–	–	–	8	20	35	–	20
4	ODP 113	696	661	Clay	525	11	60	70	45	25	1.45	2	0.55	1.65	1.85	0.2	–	–	–	27.6	25	52	63	38
5	ODP 120	748	1301	Carbonate	190	42.9	20	70	40	30	1.6	2.2	0.6	1.55	1.9	0.35	–	–	–	13.5	10	71.2	90	5.5
6	ODP 121	752	1086	Carbonate	290	60.4	20	50	30	20	1.85	2.1	0.25	2	2.45	0.45	–	–	–	14.5	15	33.9	46.1	12.5
7	ODP 127	794	2822	Clay	293.5	7.9	55	86	72	14	1.27	1.7	0.43	1.58	1.85	0.27	0.4	0.6	0.2	37.5	40	125	103	36
8	ODP 127	795	3310	Clay	326	5.3	40	80	60	20	1.55	1.85	0.3	1.55	1.85	0.3	–	–	–	43.2	40	132	113	61
9	ODP 127	796	2596	Clay	212.5	5.5	35	70	55	15	1.55	1.9	0.35	1.7	1.9	0.2	0.6	0.8	0.2	38	25	178	156	62
10	ODP 127	797	2876	Clay	303	8	45	85	65	20	1.4	1.8	0.4	1.8	2	0.2	0.4	0.6	0.2	36.9	30	121	101	49.5
11	ODP 128	798	911	Clay	451	3.4	35	65	55	10	1.7	1.85	0.15	2	2.3	0.3	0.17	0.17	0	38.8	30	83	98	121
12	ODP 128	799	2985	Clay	450	6.2	60	77	57	20	1.5	1.8	0.3	–	–	–	–	–	–	44.2	40	98	96	70
13	ODP 138	846	3387	Carbonate	370	12	40	70	60	10	1.55	1.7	0.15	1.75	1.85	0.1	0.55	0.8	0.25	16.2	20	39	37.8	15
14	ODP 138	847	3346	Carbonate	233	6.6	30	70	–	–	1.45	–	–	1.52	–	–	0.42	–	–	19.2	–	76	74.5	42
15	ODP 138	850	3798	Carbonate	215	8.5	45	75	65	10	1.45	1.55	0.1	1.55	1.65	0.1	0.6	0.65	0.05	3.2	15	7.8	8.4	64.5
16	ODP 143	869	4838	Carbonate	140	37.5	25	60	40	20	1.3	1.5	0.2	1.55	1.55	0	–	–	–	–	10	173	166.8	6.5
17	ODP 150	902	808	Clay	680	28.5	30	60	45	15	1.85	2.05	0.2	1.85	2	0.15	0.9	1	0.1	27	25	40	48	13
18	ODP 150	903	703	Clay	1050	25.5	25	65	45	20	1.7	1.9	0.2	1.8	1.9	0.1	–	–	–	42.2	40	40	–	12.5
19	ODP 150	904	577	Clay	525	31.5	20	60	50	10	1.7	1.95	0.25	1.85	2.2	0.35	1	1.5	0.5	21.2	15	40	52	12.5
20	ODP 159	959	2102	Carbonate	430	31.5	20	60	30	30	1.5	1.9	0.4	1.5	1.75	0.25	0.8	0.9	0.1	22	25	48	56.2	–
21	ODP 159	960	2060	Carbonate	140	38	10	65	40	25	1.7	1.9	0.2	1.5	1.75	0.25	0.8	0.9	0.1	8.1	30	48	52.8	–
22	ODP 159	961	3612	Carbonate	150	19.5	5	65	35	30	1.6	2.05	0.45	1.6	2.2	0.6	–	–	–	–	30	–	–	–
23	ODP 159	962	4649	Clay	55	19.5	15	70	40	30	1.4	1.8	0.4	1.55	–	–	0.2	0.25	0.05	5.8	25	15	18	10
24	ODP 167	1010	3690	Clay	180	13.1	60	73	67	6	1.5	1.7	0.2	–	–	–	–	–	–	23.4	15	122	118	15
25	ODP 167	1011	2021	Clay	205	7.5	30	65	62	3	1.62	1.64	0.02	–	–	–	0.75	–	–	24.8	15	108	111	22.5
26	ODP 167	1016	4162	Clay	282	7.2	50	75	65	10	1.4	1.65	0.25	–	–	–	0.5	0.6	0.1	30.9	–	105	88	30
27	ODP 167	1022	2325	Clay	360	8	10	65	58	7	1.55	1.75	0.2	–	–	–	0.55	0.8	0.25	33.6	–	88	84	–

1818 Appendix I. Continued.

28	ODP 177	1090	3710	Carbonate	290	35	40	83	77	6	1.6	–	–	–	–	–	–	–	–	2	15	8	7	30
29	ODP 178	1095	3863	Clay	490	6.5	20	57	45	12	1.75	1.9	0.15	1.7	1.9	0.2	0.65	0.7	0.05	16.4	20	33	–	110
30	ODP 181	1122	4432	Clay	585	15	40	52	42	10	1.85	2.05	0.2	2.3	2.5	0.2	–	–	–	–	20	–	–	20
31	ODP 182	1132	230	Carbonate	255	13.8	6	44	26	18	1.55	1.65	0.1	1.9	2.3	0.4	0.49	0.98	0.49	23.2	15	41.6	43.3	–
32	ODP 182	1133	1049	Carbonate	40	13.8	5	55	–	–	1.86	1.9	0.04	1.59	–	–	–	–	–	13.2	–	41.6	–	–
33	ODP 185	1149	5829	Clay	180	14	35	70	30	40	1.5	2	0.5	–	–	–	0.9	1.8	0.9	6.5	18	33	28.1	10
34	ODP 186	1150	2692	Clay	1050	8.3	35	65	55	10	1.55	1.7	0.15	1.8	2	0.2	1	1.4	0.4	32.3	25	28.9	20.1	70
35	ODP 188	1165	3549	Clay	600	19.5	20	60	42	18	1.75	2	0.25	1.7	1.85	0.15	0.7	0.9	0.2	19.2	15	32	51.4	13.5
36	ODP 189	1170	2716	Carbonate	475	37.5	20	60	50	10	1.65	1.8	0.15	1.7	1.9	0.2	–	–	–	27	40	52	56	10
37	ODP 189	1171	2159	Carbonate	375	42.9	30	65	45	20	1.4	1.7	0.3	1.6	1.9	0.3	0.6	2	1.4	26.3	35	62	68	8
38	ODP 189	1172	2633	Carbonate	500	44	30	60	48	12	1.55	1.75	0.2	1.85	1.9	0.05	1	1.15	0.15	25.7	30	46.6	55	18
39	ODP 190	1173	4802	Clay	344	3.5	40	65	51	14	1.6	1.8	0.2	1.7	1.8	0.1	0.3	0.55	0.25	60	35	170	180	52
40	ODP 195	1201	5721	Clay	25	4.5	–	85	55	30	1.25	1.7	0.45	1.62	2.2	0.58	–	–	–	4.8	15	125	98	3
41	ODP 198	1207	3112	Carbonate	150	16.5	25	60	55	5	1.9	2.18	0.28	1.5	1.7	0.2	0.45	0.5	0.05	–	20	–	–	5
42	ODP 201	1225	3772	Carbonate	275	13	50	80	70	10	1.45	1.55	0.1	1.52	1.55	0.03	0.55	0.65	0.1	6.3	15	17.4	15.5	43
43	ODP 201	1226	3297	Carbonate	370	13	45	78	61	17	1.55	1.7	0.15	1.75	1.8	0.05	0.55	0.75	0.2	22.9	20	57.2	48.7	16
44	ODP 206	1256	3645	Carbonate	175	12.5	35	81	68	13	1.3	1.45	0.15	1.55	1.62	0.07	0.35	0.38	0.03	27	10	146	113	27
45	DSDP 11	98	2769	Carbonate	165	51.9	25	65	60	5	1.55	1.8	0.25	1.92	1.92	0	–	–	–	–	–	–	–	6
46	DSDP 19	184	1910	Clay	600	5.3	80	65	–	–	1.5	2	0.5	1.8	2.2	0.4	–	–	–	51.2	–	82	74	–
47	DSDP 19	185	2110	Clay	640	5.3	65	60	–	–	1.6	1.75	0.15	1.63	2.02	0.39	–	–	–	35	–	50.4	42.7	–
48	DSDP 19	188	2649	Clay	550	4.5	75	70	–	–	1.35	1.8	0.45	1.6	2	0.4	–	–	–	–	–	–	–	–
49	DSDP 19	189	3437	Clay	540	4.5	20	55	–	–	1.64	2.05	0.41	1.63	2.2	0.57	–	–	–	53.7	–	95.8	–	–
50	DSDP 19	190	3875	Clay	610	5.3	40	60	–	–	1.5	–	–	1.6	–	–	–	–	–	–	–	–	–	–
51	DSDP 19	191	3854	Clay	520	3.1	25	55	–	–	1.75	2	0.25	1.75	2.05	0.3	–	–	–	–	–	–	–	–
52	DSDP 19	192	3014	Clay	600	8.5	60	60	–	–	1.55	1.9	0.35	1.5	1.7	0.2	–	–	–	–	–	–	–	–
53	DSDP 29	277	1214	Carbonate	246	38	10	85	78	7	1.28	1.52	0.24	–	–	–	–	–	–	–	–	–	–	13.5
54	DSDP 29	280	4176	Carbonate	160	33.9	45	85	–	–	1.05	–	–	–	–	–	–	–	–	–	–	–	–	39
55	DSDP 41	366	2853	Carbonate	520	42.9	35	54	34	20	–	–	–	1.9	2.3	0.4	–	–	–	–	35	–	–	19
56	DSDP 41	367	4758	Carbonate	330	42.9	20	57	42	15	–	–	–	1.6	1.71	0.11	–	–	–	–	30	–	–	6.5
57	DSDP 41	368	3366	Carbonate	355	42.9	15	64	52	12	1.65	1.8	0.15	1.7	2	0.3	–	–	–	–	35	–	–	–
58	DSDP 41	370	4214	Carbonate	425	36	10	49	33	16	–	–	–	1.84	2.14	0.3	–	–	–	–	35	–	–	8
59	DSDP 43	385	4936	Clay	165	51.9	30	82	60	22	1.42	1.65	0.23	1.54	1.74	0.2	–	–	–	–	15	–	–	27.5
60	DSDP 43	387	5117	Clay	225	42.9	20	68	41	27	1.6	1.85	0.25	1.66	1.9	0.24	–	–	–	–	20	–	–	26
61	DSDP 47	397	2900	Carbonate	700	13.8	20	57	40	17	1.7	2	0.3	1.55	1.8	0.25	–	–	–	–	15	–	–	50
62	DSDP 48	405	2958	Carbonate	265	51.9	10	65	50	15	1.45	1.65	0.2	–	1.8	–	0.8	1.1	0.3	–	15	–	–	74
63	DSDP 63	467	2128	Clay	550	8.5	50	65	35	30	1.6	1.95	0.35	1.65	2.2	0.55	–	–	–	39.2	20	63	–	87.5
64	DSDP 63	469	3790	Clay	225	13.8	50	–	42	–	1.6	1.89	0.29	1.5	2.2	0.7	–	–	–	–	–	–	–	20
65	DSDP 63	471	3101	Clay	155	11.6	55	–	30	–	1.5	1.82	0.32	1.64	1.99	0.35	–	0.3	–	22.5	–	132	119.1	20
66	DSDP 63	473	3249	Clay	181	8.5	15	63	40	23	1.51	1.73	0.22	1.56	1.98	0.42	–	–	–	13	10	64	56.2	30
67	DSDP 93	603	4633	Clay	950	36	20	54	34	20	1.85	2.1	0.25	1.7	2.1	0.4	–	–	–	41.7	10	41.8	–	35

1820 * The maximum thickness of the silica transition zone as estimated from the porosity
1821 depth profiles.
1822
1823
1824
1825
1826
1827
1828
1829
1830
1831
1832
1833
1834
1835
1836

Appendix II. Characterisation of the opal-A to opal-CT transformation, penetrated by the studied ODP and DSDP sites, using the data types described in the Section Identification of $TZ_{A/CT}$. The values were mostly extracted or derived from ODP and DSDP datasets. Values for the ODP Sites 794 and 795 were derived from Varkouhi et al. (2020b), and the limited XRD data for the DSDP Sites 184, 185, 188, 198, 190, 191, and 192 derived from Hein et al. (1978). Interstitial-chemistry data for DSDP Sites 387, 469, and 471 were derived from Hesse and Schacht (2011). No. = the identification number of the sites presented in Figure 1, Opal-CT_A = mean amount of opal-CT in the opal-A-rich sediments above the silica transition, Opal-CT_{CT} = mean amount of opal-CT in the opal-CT-rich sediments hosting the silica transition, BSi_A = mean biogenic silica in the total volume of the opal-A-rich sediments, BSi_{CT} = mean biogenic silica in the total volume of the opal-CT-rich sediments, DSi_A = mean pore-water concentration of dissolved silica in the opal-A-rich sediments, DSi_{CT} = mean pore-water concentration of dissolved silica in the opal-CT-rich sediments

No.	Site	XRD				Smear slides				Descriptive lithology		Seismic reflection		Pore-water chemistry			
		$TZ_{A/CT}$ depth, mbsf	Opal-CT_A, wt%	Opal-CT_{CT}, wt%	$TZ_{A/CT}$ thickness, m	$TZ_{A/CT}$ depth, mbsf	BSi_A, %	BSi_{CT}, %	$TZ_{A/CT}$ thickness, m	$TZ_{A/CT}$ depth, mbsf	$TZ_{A/CT}$ thickness, m	$TZ_{A/CT}$ depth, mbsf	$TZ_{A/CT}$ thickness, m	$TZ_{A/CT}$ depth, mbsf	DSi_A, µM	DSi_{CT}, µM	$TZ_{A/CT}$ thickness, m
1	642	–	–	–	–	275	35.5	0.5	–	285	40	–	–	–	–	–	–
2	643	–	–	–	–	265	61	4	38	275	–	–	–	–	–	–	–
3	647	–	–	–	–	235	49	3.5	28	245	–	–	–	–	–	–	–
4	696	523	0	24.5	–	520	61	0.1	10	470	60	520	–	510	1140	250	45
5	748	–	–	–	–	130	20.5	0.5	–	195	–	170	–	165	630	290	90
6	752	–	–	–	–	269	20	0	–	280	–	–	–	–	555	–	–
7	794	100	8	16	–	250	56	0.5	51	293	–	290	–	271	930	550	71
8	795	0	10	22	–	307	40.5	0.1	54	325	–	330	–	321	1010	690	58
9	796	215	7	18	–	180	38	4	60	224	–	215	–	177	1120	440	83
10	797	299	8	20	–	220	45.5	0.1	85	299	–	305	–	280	1005	495	90
11	798	460	0	28	–	380	39	5	95	455	–	430	–	420	1015	785	–
12	799	265	7.5	14.5	–	440	65	4.5	60	455	–	430	–	445	1150	750	–
13	846	–	0	–	–	335	40.5	0.1	40	372	–	365	–	340	1190	580	45
14	847	–	0	–	–	202	30	0	–	234	–	215	–	–	1270	–	–
15	850	–	–	–	–	202	47.5	37	–	212	–	220	–	–	970	1020	–
16	869	–	–	–	–	120	25.5	1	24	147	61	130	–	115	840	270	105
17	902	0	9	25	–	655	31	0.05	80	680	–	660	–	–	995	–	–
18	903	740	5.5	32	–	1040	27	0.1	85	1065	–	1070	–	980	840	730	–
19	904	520	0	31	–	510	20	–	–	520	–	530	–	500	980	–	–
20	959	415	0.5	32	–	410	21	4	55	427	57	440	–	375	710	520	104
21	960	111	12	33	–	100	10	0	–	136	39	145	–	–	530	470	–
22	961	123	3	42	–	120	5	0	–	148	40	–	–	–	255	160	–
23	962	48	12	43	–	51	16	8	34	47	76	55	–	–	440	–	–
24	1010	–	0	–	–	167	66	9	37	178	32	155	–	–	880	–	–
25	1011	–	0	–	–	199	35	9.5	61	202	56	200	–	–	870	1420	–
26	1016	298	0	24	–	251	53	7	45	282	35	280	–	–	1120	–	–
27	1022	–	0	–	–	–	–	–	–	362	24	340	–	–	820	–	–

Appendix II. Continued.

28	1090	296	0	15	–	258	45	15	136	292	51	285	–	265	900	760	95
29	1095	499	–	13	–	462	22	2	91	485	–	495	–	475	750	490	–
30	1122	–	0	–	–	439	42	2	170	588	30	565	–	–	765	–	–
31	1132	–	0	–	–	239	6	–	–	255	30	250	–	240	510	260	130
32	1133	45	0	6	–	30	5	–	–	43	43	50	–	–	425	605	–
33	1149	155	6.5	17	–	–	37	13	–	182	91	185	–	–	505	360	–
34	1150	0	7.5	27	–	1040	38	14	–	1047	–	–	–	–	–	–	–
35	1165	492	0	15	–	490	22	2.5	187	597	–	625	–	600	740	310	–
36	1170	450	1.5	20	–	460	21	1	43	480	–	470	–	450	875	120	55
37	1171	380	0	10	–	322	30	0	–	350	–	380	–	320	760	375	155
38	1172	505	0	9	–	503	32	2	37	505	–	520	–	495	790	460	59
39	1173	0	14	17.5	–	–	40	0	–	344	–	365	–	325	910	150	80
40	1201	35	0	3	–	–	–	–	–	24	23	30	–	–	130	310	–
41	1207	160	0	2.5	–	137	26.5	1.5	23	145	40	155	–	135	815	455	43
42	1225	275	0	10	–	260	53	8	58	276	42	–	–	–	935	810	–
43	1226	380	0	9	–	316	46	0.5	102	370	48	–	–	360	940	560	30
44	1256	190	0	9	–	160	38	10	80	185	65	–	–	175	790	745	51
45	98	–	–	–	–	–	27	9	–	180	60	–	–	–	–	–	–
46	184	600	0	–	–	600	81	2	20	598	67	620	–	–	–	–	–
47	185	650	0	–	–	605	66.5	2.5	60	645	79	–	–	–	–	–	–
48	188	585	0	–	–	565	78	3.5	25	575	63	525	–	–	–	–	–
49	189	500	–	–	–	–	20	0	–	535	–	–	–	–	–	–	–
50	190	615	0	–	–	–	41	0.5	–	600	27	605	–	–	–	–	–
51	191	625	0	–	–	–	25	0	–	525	–	505	–	–	–	–	–
52	192	700	0	–	–	620	65.5	10.5	130	625	100	–	–	–	–	–	–
53	277	–	–	–	–	–	11.5	1.5	–	250	45	–	–	–	–	–	–
54	280	–	–	–	–	–	47	4	–	140	55	–	–	–	–	–	–
55	366	–	–	–	–	–	37.5	2	–	520	40	–	–	–	–	–	–
56	367	–	–	–	–	–	22	2.5	–	330	55	305	–	–	–	–	–
57	368	–	–	–	–	–	15.5	0.1	–	360	–	–	–	–	–	–	–
58	370	–	–	–	–	–	11	2	–	450	120	365	–	–	–	–	–
59	385	–	–	–	–	–	30	0	–	165	40	–	–	–	–	–	–
60	387	–	–	–	–	200	21	0.5	32	222	–	–	–	190	445	360	–
61	397	–	–	–	–	–	21	1	–	700	50	–	–	–	–	–	–
62	405	–	–	–	–	–	10	0	–	264	36	–	–	–	–	–	–
63	467	–	–	–	–	495	50	0	–	530	45	525	–	–	–	–	–
64	469	–	–	–	–	220	55	5	160	235	60	220	–	180	790	130	75
65	471	–	–	–	–	160	60	5	80	160	140	–	–	120	710	100	290
66	473	–	–	–	–	178	17	2	75	190	60	–	–	–	–	–	–
67	603	–	–	–	–	–	21.5	1	–	960	60	930	–	–	–	–	–

Appendix III. Statistics for the $TZ_{A/CT}$ thickness (upper table) and temperature (lower table) values presented in Appendix I.

Statistical parameters	Clay-dominated sites	Carbonate-dominated sites	All studied sites
Count	28	23	51
Sum	635	520	1155
Minimum	10	10	10
Maximum	40	40	40
Range	30	30	30
Average	22.68	22.61	22.65
Averagea	22.68	22.61	22.65
Average deviation	7.7	8.6	8.11
Median	20	20	20
Mode	15	15	15
Standard deviation	9.41	9.64	9.42
Population standard deviation	9.24	9.42	9.32
Variance	88.6	92.88	88.71
Population variance	85.43	88.85	86.97
Kurtosis	-0.54	-1.4	-0.96
Skewness	0.71	0.3	0.5

Statistical parameters	Clay-dominated sites	Carbonate-dominated sites	All studied sites
Count	31	16	47
Sum	900.6	270.3	1170.9
Minimum	4.8	2	2
Maximum	60	27	60
Range	55.2	25	58
Average	29.05	16.89	24.91
Averagea	29.05	16.89	24.91
Average deviation	12.49	7.27	11.53
Median	30.9	17.7	23.4
Mode	11	27	27
Standard deviation	14.95	8.59	14.28
Population standard deviation	14.71	8.32	14.12
Variance	223.58	73.85	203.81
Population variance	216.37	69.24	199.47
Kurtosis	-0.78	-1.12	-0.45
Skewness	0.03	-0.44	0.39

1878

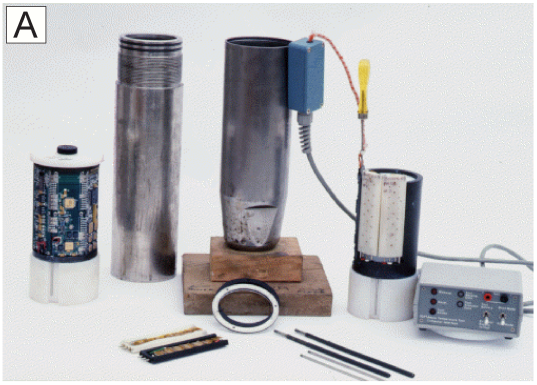

B

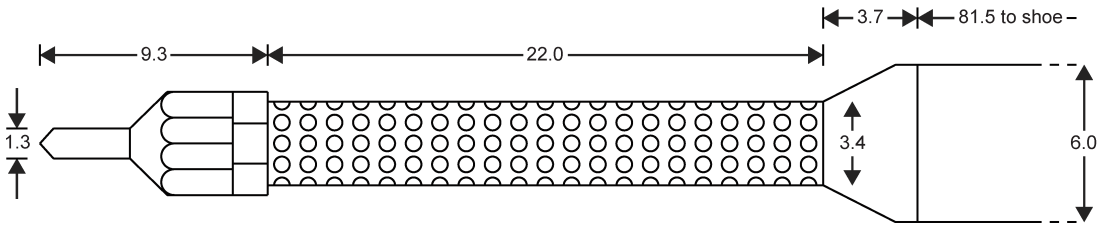

1880 Appendix IV. A) APC tool components (left to right background): APC tool on
1881 cylindrical holder, APC landing sub, APC coring shoe (with internal annular cavity),
1882 interface cable attached to another APC tool (turned to show battery packs), and
1883 interface box. (left to right in the foreground): battery packs, tool retaining rings, and
1884 extraction tools (photograph from Fisher and Becker, 1993); B) WSTP probe
1885 assembly for temperature measurement and fluid sampling. All dimensions in
1886 centimetres (redrawn and slightly modified from Fisher and Becker, 1993).
1887
1888
1889
1890
1891
1892
1893
1894
1895

93

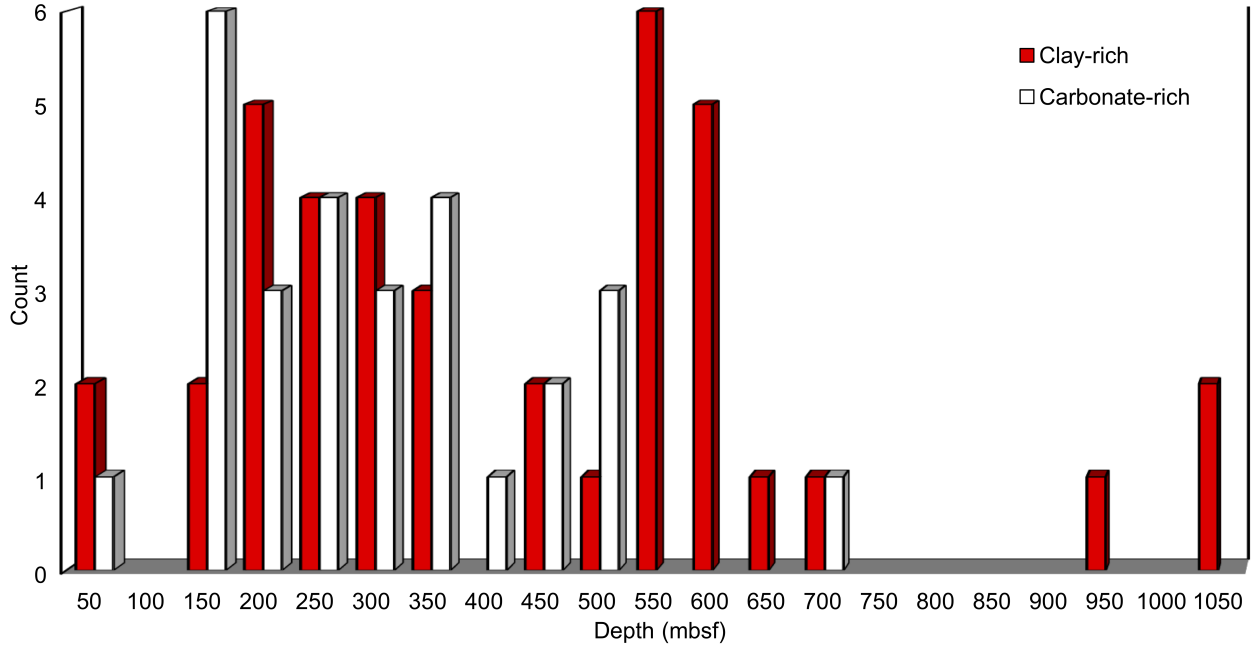

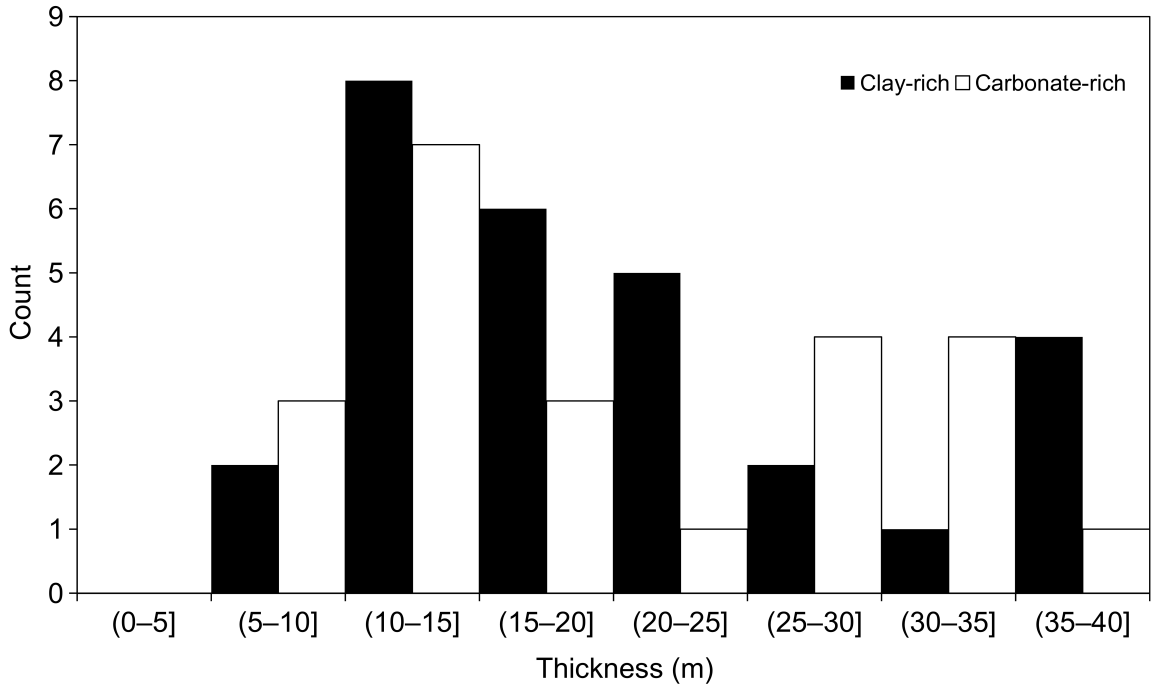

1896 Appendix V. Upper histogram showing the depth distribution of the opal-A to opal-
1897 CT transition zones in clay- and carbonate-rich lithologies drilled at the studied
1898 borehole sites. Lower histogram showing the distribution of $TZ_{A/CT}$ thickness
1899 categories for the investigated sites. Each half-open thickness interval on the abscissa
1900 also includes its upper (right hand side) end point.

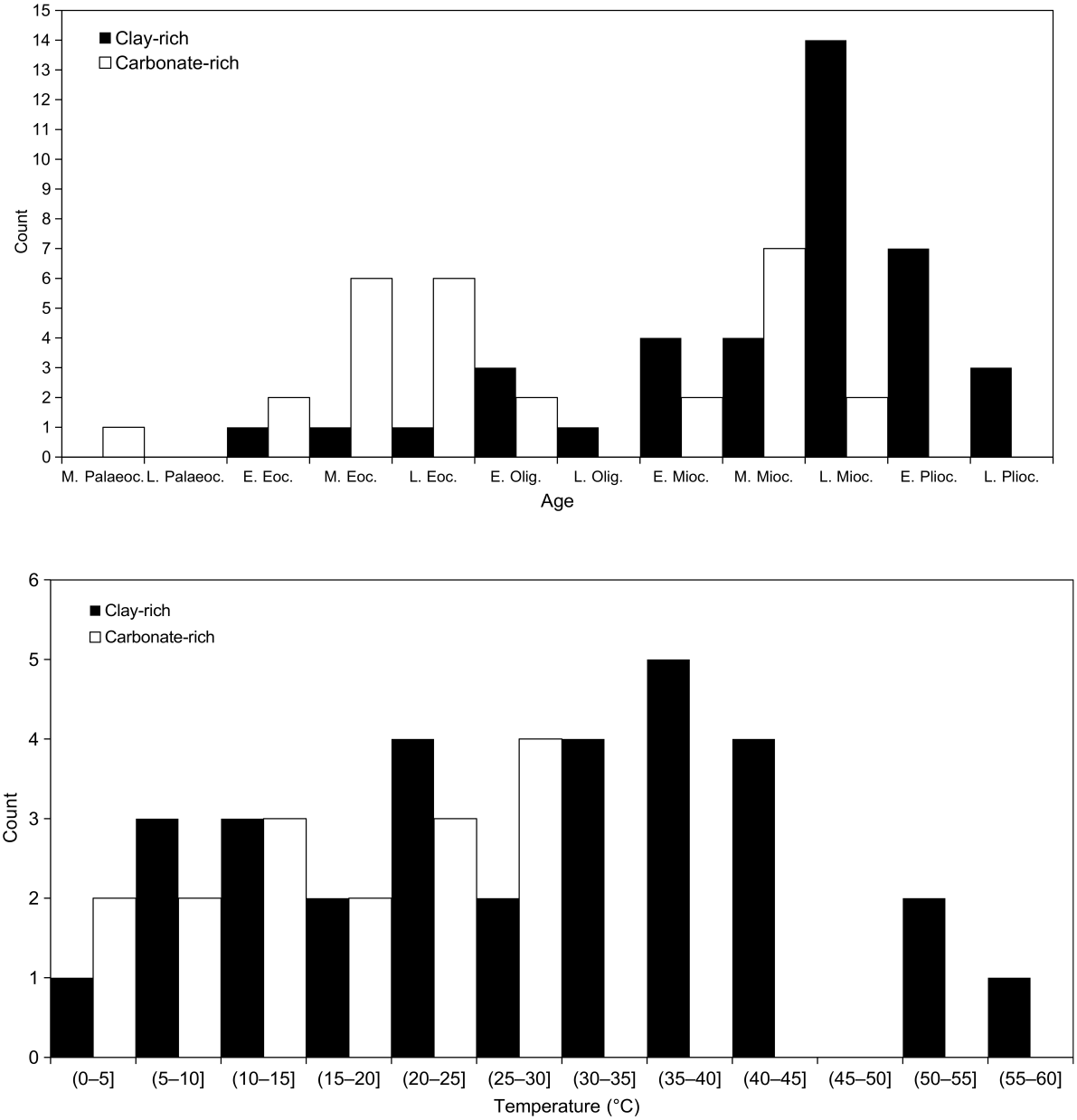

1901 Appendix VI. Upper histogram showing the age distribution of silica diagenetic
1902 transitions in the studied ODP and DSDP boreholes. The abbreviations represent: M.
1903 Palaeoc. = Middle Palaeocene, L. Palaeoc. = Late Palaeocene, E. Eoc. = Early
1904 Eocene, M. Eoc. = Middle Eocene, L. Eoc. = Late Eocene, E. Olig. = Early
1905 Oligocene, L. Oligocene = Late Oligocene, E. Mioc. = Early Miocene, M. Mioc. =
1906 Middle Miocene, L. Mioc. = Late Miocene, E. Plioc. = Early Pliocene, L. Plioc. =
1907 Late Pliocene. Lower bar graph showing the distribution of temperature at $TZ_{A/CT}$
1908 depth for the studied borehole sites. Each half-open temperature interval on the
1909 abscissa also includes its upper end point.

95

1910 Appendix VII. Thermodynamic modelling of biogenic silica diagenesis.

1911

1912 According to earlier works (e.g., Kastner et al., 1977), the transformation of opal-A
1913 to opal-CT requires the dissolution of siliceous tests into pore waters and
1914 reprecipitation of the dissolved silica, as dispersed crystalline cristobalite, within the
1915 sediment matrix (Langseth and Tamaki, 1992). The precipitation of opal-CT is the
1916 target transformation process in silica diagenesis, and is substantially influenced by
1917 the temperature–time dependent dissolution rate of biogenic silica that controls
1918 silicic acid concentrations being released into the pore solutions (e.g., Varkouhi and
1919 Wells, 2020). The dependence on temperature and time of the reaction can be
1920 described by the Arrhenius equation:

1921

1922 $$k = Ae^{\frac{-Ea}{RT}} \qquad (1.1)$$

1923

1924 where k is the first-order kinetic coefficient (in 1/m.y.), A is the pre-exponential
1925 factor (7.18×10^{13}/m.y., according to Icenhower and Dove, 2000), Ea is the
1926 activation energy (92000 J/mol; Icenhower and Dove, 2000), R is the gas constant
1927 (8.314 J/K.mol), and T is the temperature (in K).

1928

1929 There are two key parameters in this equation:
1930 a) The pre-exponential factor represents the frequency of collisions between reactant
1931 molecules of solid silica and water. Given this, A is a temperature-dependent factor
1932 because the molecular collision, and therefore the production of dissolved silica is a
1933 function of temperature. As temperature increases, these reactant molecules move
1934 faster (i.e., a higher kinetic energy) and are more likely to further collide (after
1935 Chang, 2005; Atkins and de Paula, 2006). Accordingly, Icenhower and Dove (2000)
1936 experimentally calculated a pre-exponential value of 7.18×10^{13}/m.y. for the
1937 dissolution of biogenic opal in marine sediments, which was chosen in this study for
1938 modelling of biogenic silica diagenesis.

1939

1940 b) The apparent activation energy is the minimum amount of energy required to start
1941 the chemical reaction. If the temperature is higher, the reactant opal and water
1942 molecules reach higher levels of kinetic energy, and hence the energy difference
1943 between the threshold energy and the energy of the molecules decreases. This means
1944 less activation energy needs to be supplied to the reactants to overcome the threshold
1945 energy (e.g., after Agarwal, 2019), which is a barrier for the dissolution of opal. As a
1946 consequence, the lower the activation energy, the earlier the reaction, and the higher
1947 the reaction rate. Following these correlations, the modelling approach in this study
1948 used an activation energy of 92 kJ/mol (92000 J/mol) calculated by Icenhower and
1949 Dove (2000) for the dissolution of biogenic silica during later diagenesis.

1950

1951

1952

1953

Appendix VII. Continued.

The kinetic coefficient, k, in Equation 1.1 represents the transformation rate, and it describes how fast (time function) opal-A can be transformed into opal-CT at a given temperature. Temperature controls the kinetic rate constant through stimulating the frequency of molecular collisions, which in turn affects the activation energy to initiate the silica dissolution reaction (after Dralus et al., 2015). This allows for predictions toward variations in the kinetic rate coefficient with temperature. As the ratio of the activation energy to the kinetic energy increases (i.e., the exponent E_a/RT with consideration of the negative sign behind it), the kinetic coefficient increases (Varkouhi and Wells, 2020). The first step toward the modelling of time–temperature dependent silica diagenesis is the evaluation of the silica transformation rate, which can be best estimated by *k* values. The second step is to estimate the transformation ratio that represents the relative amount of opal-A transformed to opal-CT at a certain point. This reacted opal-A content can be extracted based on the first-order rate law:

$$A = A_0 e^{-kt} \qquad (1.2)$$

where A is the amount of biogenic silica at time $t \neq 0$ (in volume %), A_0 is the initial amount of biogenic silica (in volume %), k is the rate coefficient (in 1/m.y.), and t is the elapsed time (in m.y.).

The key parameters in the rate law equation are time and the transformation rate (k), clearly illustrating the relevance of time and temperature during silica diagenetic transformation.

The transformation ratio can then be calculated using equation $k' = 1 - (A/A_0)$, where k' is the transformation ratio and A/A_0 is the relative amount of unreacted opal-A.